



## Article

# Design of an Antimatter Large Acceptance Detector In Orbit (ALADInO)

Oscar Adriani <sup>1,2</sup> , Corrado Altomare <sup>3</sup> , Giovanni Ambrosi <sup>4</sup> , Philipp Azzarello <sup>5</sup>, Felicia Carla Tiziana Barbato <sup>6,7</sup> , Roberto Battiston <sup>8,9</sup> , Bertrand Baudouy <sup>10</sup> , Benedikt Bergmann <sup>11</sup> , Eugenio Berti <sup>1,2</sup> , Bruna Bertucci <sup>12,4</sup> , Mirko Boezio <sup>13,14</sup> , Valter Bonvicini <sup>13</sup> , Sergio Bottai <sup>2</sup> , Petr Burian <sup>11</sup> , Mario Buscemi <sup>15,16</sup> , Franck Cadoux <sup>5</sup>, Valerio Calvelli <sup>17,†</sup> , Donatella Campana <sup>18</sup>, Jorge Casaus <sup>19</sup>, Andrea Contin <sup>20,21</sup>, Raffaello D'Alessandro <sup>1,2</sup> , Magnus Dam <sup>22</sup> , Ivan De Mitri <sup>6,7</sup> , Francesco de Palma <sup>23,24</sup>, Laurent Derome <sup>25</sup> , Valeria Di Felice <sup>26</sup>, Adriano Di Giovanni <sup>6,7</sup> , Federico Donnini <sup>4</sup> , Matteo Duranti <sup>4,\*</sup> , Emanuele Fiandrini <sup>12,4</sup> , Francesco Maria Follega <sup>8,9</sup> , Valerio Formato <sup>26</sup> , Fabio Gargano <sup>3</sup> , Francesca Giovacchini <sup>19</sup>, Maura Graziani <sup>12,4</sup> , Maria Ionica <sup>4</sup> , Roberto Iuppa <sup>8,9</sup> , Francesco Loparco <sup>27,3</sup> , Jesús Marín <sup>19</sup>, Samuele Mariotto <sup>28,22</sup> , Giovanni Marsella <sup>15,16</sup> , Gustavo Martínez <sup>19</sup>, Manel Martínez <sup>29</sup>, Matteo Martucci <sup>30,26</sup> , Nicolò Masi <sup>21</sup>, Mario Nicola Mazziotta <sup>3</sup> , Matteo Mergé <sup>30,26</sup> , Nicola Mori <sup>2</sup> , Riccardo Munini <sup>13</sup>, Riccardo Musenich <sup>17</sup> , Lorenzo Mussolin <sup>12,4</sup> , Francesco Nozzoli <sup>9</sup> , Alberto Oliva <sup>21</sup> , Giuseppe Osteria <sup>18</sup>, Lorenzo Pacini <sup>2</sup> , Mercedes Paniccia <sup>5</sup>, Paolo Papini <sup>2</sup> , Mark Pearce <sup>31</sup>, Chiara Perrina <sup>32</sup>, Piergiorgio Picozza <sup>33,30,26</sup> , Cecilia Pizzolotto <sup>13</sup> , Stanislav Pospíšil <sup>11</sup> , Michele Pozzato <sup>21</sup>, Lucio Quadrani <sup>20,21</sup>, Ester Ricci <sup>8,9</sup> , Javier Rico <sup>29</sup>, Lucio Rossi <sup>28,22</sup> , Enrico Junior Schioppa <sup>23,24</sup> , Davide Serini <sup>3</sup> , Petr Smolyanskiy <sup>11</sup> , Alessandro Sotgiu <sup>30,26</sup> , Roberta Sparvoli <sup>30,26</sup> , Antonio Surdo <sup>24</sup>, Nicola Tomassetti <sup>12,4</sup> , Valerio Vagelli <sup>34,4,\*</sup> , Miguel Ángel Velasco <sup>19</sup>, Xin Wu <sup>5</sup> and Paolo Zuccon <sup>8,9</sup>



**Citation:** Adriani, O.; Altomare, C.; Ambrosi, G.; Azzarello, P.; Barbato, F.C.T.; Battiston, R.; Baudouy, B.; Bergmann, B.; Berti, E.; Bertucci, B.; et al. Design of an Antimatter Large Acceptance Detector In Orbit (ALADInO). *Instruments* **2022**, *6*, 19. <https://doi.org/10.3390/instruments6020019>

Academic Editor: Antonio Ereditato

Received: 17 January 2022

Accepted: 15 April 2022

Published: 11 May 2022

**Publisher's Note:** MDPI stays neutral with regard to jurisdictional claims in published maps and institutional affiliations.



**Copyright:** © 2022 by the authors. Licensee MDPI, Basel, Switzerland. This article is an open access article distributed under the terms and conditions of the Creative Commons Attribution (CC BY) license (<https://creativecommons.org/licenses/by/4.0/>).

- <sup>1</sup> Dipartimento di Fisica e Astronomia, Università degli Studi di Firenze, IT-50019 Sesto Fiorentino (Firenze), Italy; oscar.adriani@unifi.it (O.A.); eugenio.berti@unifi.it (E.B.); raffaello.dalessandro@unifi.it (R.D.)
- <sup>2</sup> Istituto Nazionale Fisica Nucleare (INFN)—Sezione di Firenze, IT-50019 Sesto Fiorentino (Firenze), Italy; sergio.bottai@fi.infn.it (S.B.); nicola.mori@fi.infn.it (N.M.); lorenzo.pacini@fi.infn.it (L.P.); paolo.papini@fi.infn.it (P.P.)
- <sup>3</sup> Istituto Nazionale Fisica Nucleare (INFN)—Sezione di Bari, IT-70126 Bari, Italy; corrado.altomare@ba.infn.it (C.A.); fabio.gargano@ba.infn.it (F.G.); marionicola.mazziotta@ba.infn.it (M.N.M.); davide.serini@ba.infn.it (D.S.)
- <sup>4</sup> Istituto Nazionale Fisica Nucleare (INFN)—Sezione di Perugia, IT-06100 Perugia, Italy; giovanni.ambrosi@pg.infn.it (G.A.); federico.donnini@pg.infn.it (F.D.); maria.ionica@pg.infn.it (M.I.)
- <sup>5</sup> Département de Physique Nucléaire et Corpusculaire, Université de Genève, CH-1211 Genève, Switzerland; philipp.azzarello@unige.ch (P.A.); franck.cadoux@unige.ch (F.C.); mercedes.paniccia@unige.ch (M.P.); xin.wu@unige.ch (X.W.)
- <sup>6</sup> Gran Sasso Science Institute (GSSI), IT-67100 L'Aquila, Italy; felicia.barbato@gssi.it (F.C.T.B.); ivan.demitri@gssi.it (I.D.M.); adriano.digiovanni@gssi.it (A.D.G.)
- <sup>7</sup> Istituto Nazionale Fisica Nucleare (INFN)—Laboratori Nazionali del Gran Sasso (LNGS), IT-67100 Assergi (L'Aquila), Italy
- <sup>8</sup> Dipartimento di Fisica, Università di Trento, IT-38123 Povo (Trento), Italy; roberto.battiston@unitn.it (R.B.); francesco.follega@unitn.it (F.M.F.); roberto.iuppa@unitn.it (R.I.); ester.ricci@unitn.it (E.R.); paolo.zuccon@unitn.it (P.Z.)
- <sup>9</sup> Istituto Nazionale Fisica Nucleare (INFN)—Trento Institute for Fundamental Physics and Applications (TIFPA), IT-38123 Povo (Trento), Italy; francesco.nozzoli@tifpa.infn.it
- <sup>10</sup> Département des Accélérateurs, de la Cryogénie et du Magnétisme, Université Paris-Saclay, CEA, FR-91191 Gif-sur-Yvette (Essonne), France; bertrand.baudouy@cea.fr
- <sup>11</sup> Institute of Experimental and Applied Physics, Czech Technical University, CZ-11000 Prague, Czech Republic; benedikt.bergmann@utef.cvut.cz (B.B.); petr.burian@utef.cvut.cz (P.B.); stanislav.pospisil@utef.cvut.cz (S.P.); petr.smolyanskiy@utef.cvut.cz (P.S.)
- <sup>12</sup> Dipartimento di Fisica e Geologia, Università degli Studi di Perugia, IT-06100 Perugia, Italy; bruna.bertucci@unipg.it (B.B.); emanuele.fiandrini@unipg.it (E.F.); maura.graziani@unipg.it (M.G.); lorenzo.mussolin@unipg.it (L.M.); nicola.tomassetti@unipg.it (N.T.)
- <sup>13</sup> Istituto Nazionale Fisica Nucleare (INFN)—Sezione di Trieste, IT-34149 Trieste, Italy; mirko.boezio@ts.infn.it (M.B.); walter.bonvicini@ts.infn.it (V.B.); riccardo.munini@ts.infn.it (R.M.); cecilia.pizzolotto@ts.infn.it (C.P.)
- <sup>14</sup> Institute for Fundamental Physics of the Universe (IFPU), IT-34014 Trieste, Italy

- <sup>15</sup> Dipartimento di Fisica e Chimica, Università degli Studi di Palermo, IT-90133 Palermo, Italy; mario.buscemi01@unipa.it (M.B.); giovanni.marsella@unipa.it (G.M.);
- <sup>16</sup> Istituto Nazionale Fisica Nucleare (INFN)—Sezione di Catania, IT-95123 Catania, Italy
- <sup>17</sup> Istituto Nazionale Fisica Nucleare (INFN)—Sezione di Genova, IT-16146 Genova, Italy; valerio.calvelli@cea.fr (V.C.); riccardo.musenich@ge.infn.it (R.M.)
- <sup>18</sup> Istituto Nazionale Fisica Nucleare (INFN)—Sezione di Napoli, IT-80126 Napoli, Italy; donatella.campana@na.infn.it (D.C.); giuseppe.osteria@na.infn.it (G.O.)
- <sup>19</sup> Centro de Investigaciones Energéticas, Medioambientales y Tecnológicas (CIEMAT), ES-28040 Madrid, Spain; jorge.casaus@ciemat.es (J.C.); francesca.giovacchini@ciemat.es (F.G.); jesus.marin@ciemat.es (J.M.); gustavo.martinez@ciemat.es (G.M.); miguelangel.velasco@ciemat.es (M.Á.V.)
- <sup>20</sup> Dipartimento di Fisica e Astronomia, Università di Bologna, IT-40100 Bologna, Italy; andrea.contin@unibo.it (A.C.); lucio.quadrani@unibo.it (L.Q.)
- <sup>21</sup> Istituto Nazionale Fisica Nucleare (INFN)—Sezione di Bologna, IT-40126 Bologna, Italy; michele.pozzato@bo.infn.it (M.P.); nicolo.masi@bo.infn.it (N.M.); alberto.oliva@bo.infn.it (A.O.)
- <sup>22</sup> Istituto Nazionale Fisica Nucleare (INFN)—Sezione di Milano, IT-20133 Milano, Italy; magnus.dam@mi.infn.it
- <sup>23</sup> Dipartimento di Matematica e Fisica, Università del Salento, IT-73100 Lecce, Italy; francesco.depalma@unisalento.it (F.d.P.); enrico.schioppa@unisalento.it (E.J.S.)
- <sup>24</sup> Istituto Nazionale Fisica Nucleare (INFN)—Sezione di Lecce, IT-73100 Lecce, Italy; antonio.surdo@le.infn.it
- <sup>25</sup> LPSC-IN2P3 (CNRS), Grenoble INP, Université Grenoble Alpes, FR-38000 Grenoble, France; laurent.derome@lpsc.in2p3.fr
- <sup>26</sup> Istituto Nazionale Fisica Nucleare (INFN)—Sezione di Roma Tor Vergata, 00133 Roma, Italy; valeria.difelice@roma2.infn.it (V.D.F.); valerio.formato@roma2.infn.it (V.F.)
- <sup>27</sup> Dipartimento di Fisica, Università e Politecnico di Bari, IT-70126 Bari, Italy; francesco.loparco@uniba.it
- <sup>28</sup> Laboratorio LASA, Università degli Studi di Milano, IT-20056 Segrate (Milano), Italy; samuele.mariotto@mi.infn.it (S.M.); lucio.rossi@mi.infn.it (L.R.)
- <sup>29</sup> Institut de Física d'Altes Energies (IFAE), Barcelona Institute of Science and Technology (BIST), ES-08193 Bellaterra (Barcelona), Spain; martinez@ifae.es (M.M.); jric@ifae.es (J.R.)
- <sup>30</sup> Dipartimento di Fisica, Università degli Studi di Roma "Tor Vergata", IT-00133 Roma, Italy; matteo.martucci@roma2.infn.it (M.M.); matteo.merge@roma2.infn.it (M.M.); piergiorgio.picozza@roma2.infn.it (P.P.); alessandro.sotgiu@roma2.infn.it (A.S.); roberta.sparvoli@roma2.infn.it (R.S.)
- <sup>31</sup> Department of Physics, KTH Royal Institute of Technology, SE-10691 Stockholm, Sweden; pearce@kth.se
- <sup>32</sup> Institute of Physics, Ecole Polytechnique Fédérale de Lausanne (EPFL), CH-1015 Lausanne, Switzerland; chiara.perrina@epfl.ch
- <sup>33</sup> Faculty of Engineering, Università Telematica Internazionale UniNettuno, IT-00186 Roma, Italy
- <sup>34</sup> Agenzia Spaziale Italiana (ASI), IT-00133 Roma, Italy
- \* Correspondence: matteo.duranti@pg.infn.it (M.D.); valerio.vagelli@asi.it (V.V.)
- † Current address: Département des Accélérateurs, de la Cryogénie et du Magnétisme, Université Paris-Saclay, CEA, FR-91191 Gif-sur-Yvette (Essonne), France.

**Abstract:** A new generation magnetic spectrometer in space will open the opportunity to investigate the frontiers in direct high-energy cosmic ray measurements and to precisely measure the amount of the rare antimatter component in cosmic rays beyond the reach of current missions. We propose the concept for an Antimatter Large Acceptance Detector In Orbit (ALADInO), designed to take over the legacy of direct measurements of cosmic rays in space performed by PAMELA and AMS-02. ALADInO features technological solutions conceived to overcome the current limitations of magnetic spectrometers in space with a layout that provides an acceptance larger than  $10 \text{ m}^2 \text{ sr}$ . A superconducting magnet coupled to precision tracking and time-of-flight systems can provide the required matter–antimatter separation capabilities and rigidity measurement resolution with a Maximum Detectable Rigidity better than 20 TV. The inner 3D-imaging deep calorimeter, designed to maximize the isotropic acceptance of particles, allows for the measurement of cosmic rays up to PeV energies with accurate energy resolution to precisely measure features in the cosmic ray spectra. The operations of ALADInO in the Sun–Earth L2 Lagrangian point for at least 5 years would enable unique revolutionary observations with groundbreaking discovery potentials in the field of astroparticle physics by precision measurements of electrons, positrons, and antiprotons up to 10 TeV and of nuclear cosmic rays up to PeV energies, and by the possible unambiguous detection and measurement of low-energy antideuteron and antihelium components in cosmic rays.

**Keywords:** cosmic rays; antimatter; dark matter; particle detectors; space instrumentation

Direct access to precision measurement of cosmic rays (CR) in space has opened a unique window to investigate the mechanisms of fundamental physics, particle physics, and the Universe in an approach that is complementary to that pursued in ground-based laboratories and particle accelerators, and provides distinctive information in the multimes-senger searches towards the understanding of the Cosmos. Indeed, the operation of particle detectors in space since the late 2000s such as Fermi-LAT [1], PAMELA [2], AMS-01 [3], AMS-02 [4], DAMPE [5], CALET [6], NUCLEON [7], and ISS-CREAM [8] have paved the way for the modern era of precision particle physics in space. These space missions have been providing groundbreaking information on CRs with energies larger than hundreds of MeV that not only have consolidated previous observations, but have also revealed unexpected phenomena not accommodated in the current models that explain the origin, acceleration, and propagation of CRs [9].

The most recent striking evidences for many unpredicted structures in the CR spectra and for an overabundance of antimatter in CRs up to TeV energies have been provided by the magnetic spectrometer detectors PAMELA [2] and AMS-02 [4], taking advantage of their excellent particle identification capabilities and of the separation of matter from antimatter particles with their spectrometers, in an approach first pioneered in space by the AMS-01 mission. However, only upper limits on the abundance of antimatter in CRs heavier than antiprotons have been set so far [10], as consequence of the finite capabilities of operating first-generation spectrometer detectors, de facto limiting our understanding of the matter–antimatter asymmetries in CRs.

Magnetic spectrometers reconstruct the trajectory of charged particles in their magnetic volume to infer the particle rigidity ( $R = p/(Ze)$ , i.e., the ratio of the particle momentum  $p$  to the particle charge  $Ze$ ) and the sign of the electric charge, thus opening the possibility to separate matter from antimatter CRs to measure the mass of the particle and to provide a redundant, independent estimation of the particle energy to that provided by calorimeters. The capability to separate matter from antimatter is clearly not accessible by calorimeter-based space-borne experiments. In order to enable a revolutionary progress towards the understanding of CR physics and, in particular, of the antimatter CR physics, a novel concept for a second-generation spectrometer detector in space is required.

The high-energy CR flux  $\Phi(E)$  features a strong energy dependence  $\Phi(E) \propto E^{-\gamma}$  with  $\gamma \approx 3$  above tens of GeV, which corresponds to a collected statistics per bin (e.g., logarithmic) roughly of  $N(E) \propto \int \Phi(E) dE \propto E^{-\gamma+1}$ . The expected abundance of GeV energy heavy antimatter produced in CR collisions is very small, out of reach for the sensitivity of currently operating detectors in space. An increase in the detector gathering power by at least two orders of magnitude together with an improvement in the detector Maximum Detectable Rigidity, MDR (value of rigidity  $R$  at which the relative error on the rigidity itself is 100%,  $\Delta R/R = 1$ ), of at least of one order of magnitude with respect to the most performing spectrometer experiment operating in space, AMS-02, are consequently the minimum requirements that should drive the efforts to develop the next-generation spectrometer detector in space. The state-of-the-art technology currently adopted in space does not entirely fulfill these requirements. To enable this scenario, the deployment in space of a magnetic spectrometer based on a superconducting magnet, a solution successfully pioneered by the BESS balloon-borne superconducting solenoidal magnet spectrometer [11] and that has never been operated for long-term space missions [12,13], is currently the most promising solution.

In this work, we discuss the design of a magnetic spectrometer to be operated outside of the geomagnetic field to advance the measurements of antimatter CRs in space. The core of the instrument will be based on a superconducting toroidal magnet made of High-Temperature Superconductor coils and a precision tracking system inside the magnetic field volume, surrounded by a time-of-flight (ToF) system. The spectrometer is designed

for precision measurements of the particle rigidity and matter–antimatter separation up to 20 TV with an acceptance larger than  $10\text{ m}^2\text{sr}$ . An isotropic 3D imaging calorimeter in the center of the instrument integrates the detector capabilities with precision energy measurements and e/p separation capabilities. The concept is optimized for a lightweight, yet accurate, instrument for operation in Earth–Sun Lagrange Point L2 delivered using a space vector technology that is already available today.

In this document, we first review the current experimental scenario for direct CR measurements in Section 1. We briefly discuss in Section 2 the latest results achieved in the physics of CRs, the open challenges, and the out-of-reach observations that could be tackled by the operation of a new generation magnetic spectrometer in space. We then provide in Section 3 the rationale of the ALADInO concept and discuss the observational prospects that could be enabled by its operations in space. We provide in Section 4 a detailed overview of possible technological solutions for the ALADInO detectors. We conclude in Section 5 with a brief discussion of possible outlooks to enable the opportunity for the ALADInO mission in L2.

## 1. Instruments for Direct Detection of Cosmic Rays in Space

Most of the scientific results described in the previous section have been achieved by precision particle physics measurements with detectors operated in space.

The concepts of high-energy CR space-borne detectors depend on their scientific targets. Most of the detectors feature an imaging calorimeter used to sample the development of the shower initiated by the CR to measure its energy, incoming direction, and identify the rare  $e^\pm$  component by the topological analysis of the shower development. The detector may be integrated with a pair-conversion tracking system to measure the incoming direction of gamma-rays converting before the calorimeter. This is the concept that has driven the design of the satellite-borne detectors Fermi-LAT and DAMPE and of the CALET detector onboard the ISS, which are the most advanced calorimetric CR detectors operating in space.

In addition to the calorimeter, the detector may feature a spectrometer, which is a tracking system in a magnetic field and surrounded by a ToF system, and is used to measure the deflection of the particle trajectory and, consequently, infer the particle rigidity  $R$  and the sign of the charge of the particle. Additional instruments, such as Cherenkov detectors [14], neutron detectors [15,16], or transition radiation detectors [17–19] are used to improve the particle identification capabilities.

While calorimetric detectors can have larger exposed area and field-of-view resulting in a larger gathering power than that of magnetic spectrometric detectors with similar sizes, they cannot separate matter from antimatter particles solely based on the information of the interactions of incoming particles in the detector. Fermi-LAT has been able to separate electrons from positrons in peculiar orbital configurations using the information on the geomagnetic field [20], but this approach is limited by the finite knowledge of the details of the geomagnetic field and by its maximum energy reach, and cannot be considered competitive with a direct charge sign measurement made with a spectrometric detector. Besides different approaches, such as the analysis of the decay signatures of exotic atoms created by capture of antinuclei from the atoms of the detector materials that is being pioneered by the GAPS mission [21] and also exploited in the GRAMS proposal [22], and the investigating studies to use high-pressure He target for the identification of antideuterons in space [23], precision measurements of the rare antimatter components in CRs can be achieved, as of today, only with the direct measurement of the CR charge sign with a magnetic spectrometer. Moreover, the aforementioned approaches are limited to the GeV and sub-GeV energy range, and cannot be used to extend the measurement of antiprotons towards and above the TeV range.

The current generation of space detectors is based on the experience of the first stratospheric balloon missions (e.g., [24–26]) and space missions (see [27] for a recent review). Magnetic spectrometry is a technique well-established in space by the successful operations

of the AMS-01 prototype, which for the first time has proven the feasibility of measurements of high-energy CRs in space with a large acceptance instrument, using a permanent magnet to generate the magnetic volume [28]. The AMS-01 heritage has been further consolidated to achieve precision measurements with the PAMELA satellite detector (2006–2016) [29] and with the AMS-02 detector onboard the International Space Station (ISS) since 2011 [12]. Both PAMELA and AMS-02 feature permanent dipolar magnets to generate the magnetic volumes of their spectrometer [29,30]. As of today, AMS-02 is the only magnetic spectrometer operating in space, and no other spectrometric mission is currently planned.

The performances of spectrometric experiments are usually represented in the literature by few figures of merits: (i) the MDR; (ii) the charge confusion (CC), which is the probability to reconstruct the opposite sign of the charge and determines the amount of electrons (hadrons) that contaminates the sample of the less-abundant positrons (antihadrons) component; (iii) the gathering power, measured as the product of the detector acceptance with the detector-integrated livetime, which depends on the detector effective area, angular aperture, selection efficiency, and operation duty cycle, and determines the amount of data collected by the instrument.

Despite the various successful missions for measurement of CRs in space, many open issues limit our understanding of the origin, acceleration, and propagation mechanisms of CRs. Proposals for instruments for the measurement of high-energy CRs in the TeV–PeV energy range include the all-calorimetric HERD instrument onboard the Chinese Space Station [31] and the spectrometric instrument AMS-100 proposed for operations in Earth–Sun Lagrange Point L2 [32]. Figure 1 reports a summary of the most relevant operating and planned instruments for measurement of high-energy CRs in space.

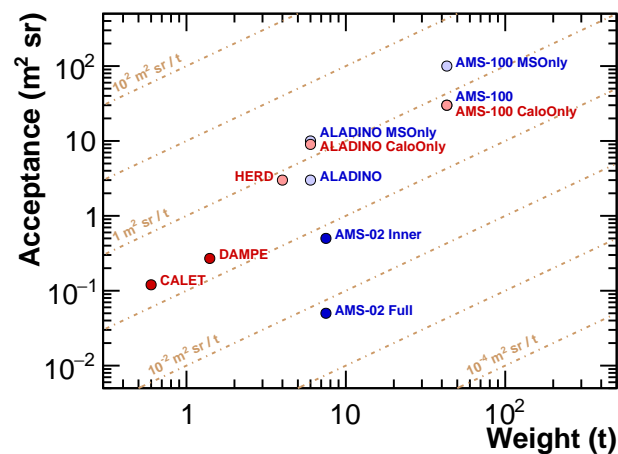


**Figure 1.** Acceptance and weight for the most relevant operating (full dots) and proposed (shaded dots) instruments for measurement of high-energy CRs in space. Blue and red dots represent, respectively, spectrometric and calorimetric instruments. The values reported in the picture are from [33] (CALET), [34,35] (DAMPE), [36–39] (AMS-02), [40] (HERD), [32] (AMS-100). The values of acceptance may depend on the analysis to which they are referred, and shall be considered as a benchmark value only. For AMS-02, the values are reported separately for particles in the acceptance of the AMS-02 inner tracker (AMS-02 Inner) or of the AMS-02 full tracker (AMS-02 Full). For ALADINO and AMS-100, the values are reported separately for particles in the acceptance of the magnetic spectrometer and calorimeter, of the magnetic spectrometer only (MSONly), and of the calorimeter only (CaloOnly). NB: this picture does not provide the full set of information to determine the final performances of each detector, because other factors (such as the spectrometer MDR or the calorimeter depth and geometry) should be taken into account. For example, for the high-energy  $e^\pm$  measurement, ALADINO is to be compared with AMS-02 Full, which is the AMS-02 configuration with the largest MDR.



In this work, we discuss a possible concept for a second-generation space-borne spectrometer, optimized for transport and operation in Earth–Sun Lagrange Point L2 using a space vector already accessible today, to drastically improve the reach of current measurements, and especially explore the frontier physics in antimatter CRs.

## 2. Frontier Physics in Charged Cosmic Rays

Revealing the details of baryogenesis and understanding the matter–antimatter asymmetry observed today in our Universe is one of the most challenging, yet intriguing, open targets of modern physics. Ground-based experiments have achieved unprecedented results that are improving our understanding of antimatter production, interactions, and spectrometry. Nonetheless, we still lack the experimental evidence of a robust mechanism that explains baryogenesis and the amount of antimatter observed in the Universe (see [41,42] and the “Big-Bang cosmology” review in [43]). Complementary direct observation of antimatter in the cosmic radiation has the potential to provide independent and groundbreaking information towards solving these and other open issues [44].

Antimatter particles are only a tiny fraction of CRs, amounting to a detected fraction of the order of  $10^{-4}$  for  $e^+$  [45,46] and  $\bar{p}$  [47]. Despite the efforts to search for nuclear antimatter in CRs in the last 20 years [2,48,49], no evidence of heavier antimatter, such as  $\bar{D}$  or  $\bar{\text{He}}$ , has directly been observed in space, and our current understanding sets upper limits, respectively, to  $10^{-7}$  for  $\bar{D}/D$  and  $10^{-8}$  for  $\bar{\text{He}}/\text{He}$ .

The detection of heavy antimatter such as  $\bar{\text{He}}$  would represent a groundbreaking, unprecedented observation with manifold implications in our understanding of baryogenesis and on the evolution of the early Universe. Production of heavy antimatter in CR collisions, for nuclear species above  ${}^3\text{He}$ , is suppressed below the sensitivity of current experiments. Roughly, the recent models for antimatter production in CR interactions predict relative abundances that decrease by a factor of  $10^{-3}$ – $10^{-4}$  per every added antinucleon [42,50], resulting in an expected ratio of  $\bar{\text{He}}/\bar{p}$  of  $10^{-10}$ . Recently, the AMS collaboration has shown, at conferences,  ${}^3\text{He}$  and  ${}^4\text{He}$  candidates, corresponding to a rate of one  $\bar{\text{He}}$  event per  $10^8$  He events or to one  $\bar{\text{He}}$  event per year for the AMS-02 gathering capabilities [51], which is in reach only for the most optimistic astrophysics  $\bar{\text{He}}$  production models [52] and, consequently, very difficult to explain in our most detailed framework of CR origin, acceleration, and propagation. In either case in which the AMS collaboration will publish the details of this observation after thorough understanding of the detector uncertainties or this hint may not be confirmed, a second-generation spectrometric mission will provide the required, independent confirmation of this finding and further push the limit down to the current expectations.

Properties of light antimatter in CRs (i.e.,  $e^+$ ,  $\bar{p}$ ,  $\bar{D}$ ,  $\bar{\text{He}}$ ) are strictly connected to the search for Dark Matter (DM). The existence of DM is largely supported by cosmological observations with intriguing hints on its particle nature, but despite the long-term effort pursued in DM production experiments at colliders and in direct DM searches, no clear evidence of DM existence and of its nature has been achieved (see the “Dark Matter” review in [43] and references therein). Indirect information on DM provided by observations from space represents a unique, complementary window to unveil the properties of DM. Light antimatter is the most promising channel to investigate in charged CRs as consequence of its larger signal yield from DM annihilation or decay with respect to the astrophysical production from CR collisions.

The operation of CR spectrometers in space has paved the way to precision measurements of the rare antimatter components in CRs. Positrons, which are the most abundant antimatter component in CRs, have raised widespread interest in the community after PAMELA first measured a hint of an excess over the expected astrophysical background above 10 GeV [53] that has been first confirmed and further extended towards TeV energies by the measurements from AMS-02 [46,54,55]. As of today, there is evidence of an undoubted excess of antimatter in the  $e^{+/-}$  channel that cannot be explained in the standard scenario of CR origin, acceleration, and propagation (see, e.g., [56]). As of today,

it is widely recognized that a modification of the CR acceleration, propagation, and interaction mechanisms [56–58] or a primary source of  $e^+$  and  $e^-$  is required to explain that excess. In the latter case, its origin is explained with DM annihilation/decay [59–67] or with production in nearby astrophysical sources such as pulsars or supernova remnants [68–76]. The outstanding, yet finite capabilities of AMS-02 in terms of gathering power and bending power will hardly enable the possibility to disentangle which is the dominant source for the positron excess, and only a second-generation spectrometric mission will feature the requirements to precisely profile the spectral features of  $e^+$  excess in the TeV energies. Additional measurements on the presence of a preferred direction in the arrival direction of high-energy  $e^{+/-}$  would provide independent hints towards the identification of localized, nearby astrophysical objects as possible dominating sources of the observed antimatter excess [77,78], providing further information to finally solve this long-standing puzzle.

Complementary information can be provided from light hadronic antimatter measurements (i.e.,  $\bar{p}$  and  $\bar{D}$ ). However, no clear indication on unexpected physics has been found so far in these channels. The latest measurement of antiprotons from AMS-02 [47] is at the limit of compatibility with the expected yield from astrophysical production in most of the energy range [79,80], although some tantalizing hints of excesses at low energies are being discussed [81–84]. The high level of similarity of the high-energy  $e^+$ ,  $p$ , and  $\bar{p}$  spectral shapes despite their different interaction and production mechanisms have also raised widespread discussion on whether the standard scenario for CR transport mechanisms should be revised [57]. To investigate possible DM signatures in the high-energy antiproton spectrum, the available measurements must be extended above the TeV energies, and a more robust estimation on the astrophysical background contribution to the antiproton flux must be produced [85–87].

Differently from antiprotons, which feature a relatively strong yield of astrophysical production background,  $\bar{D}$  and  ${}^3\bar{\text{He}}$  have never been observed in CRs. They feature, however, a much larger sensitivity to a GeV-energy DM-induced signal, as their astrophysical background is highly suppressed by kinematics in this region [88–91]. Although the  $\bar{D}$  yield is barely in reach of current spectrometric experiments in space, even in the most promising model scenarios, a second-generation spectrometric mission will be able to gather enough statistics to shed light on this unexplored sensitivity region. Together with possible evidences of low-energy light antimatter excesses found in CRs from alternative measurement approaches (e.g., GAPS, GRAMS, or ADHD, see Section 1), the undisputed detection of  $\bar{D}$  and possibly  ${}^3\bar{\text{He}}$  in CRs would provide unprecedented knowledge on the physics of DM, while a nondetection would strongly limit wide ranges of models and provide important inputs to other DM search efforts. The detection of antimatter CRs outside of the geomagnetic field region would strongly limit the systematic uncertainties in the measurement from secondary trapped anti-CRs and reduce the statistical uncertainty especially at low energies, strongly improving the robustness and extent of the measurement.

The precision study of CR antimatter clearly requires a strong assessment of the astrophysical background. At high energies, where the model predictions are mostly limited by our finite understanding of the primary particle spectra and their interaction cross sections with the interstellar medium, complementary measurements of high-energy CRs from protons up to the supra-Fe elements and electrons and improved estimations of cross section at very high energies by ground-based experiments are required. Important input will be also provided by improved models of antimatter production dynamics, such as those from ground-based antimatter facilities and collider experiments. Finally, evidence of DM signals at energies below tens of GeV may be hidden by the short- and long-term effects of solar activity in the flux of CRs. Improving our best understanding of these factors with a campaign of low- and high-energy CR flux measurements, as well as gathering all required inputs from complementary facilities on the ground, is a mandatory objective of next-generation spectrometric missions.

### 3. Design for an Antimatter Large Acceptance Detector In Orbit (ALADInO)

ALADInO is a mission concept mainly designed to tackle the open points and explore the frontier of antimatter physics in CRs to provide revolutionary and unprecedented observations of CRs in space. The instrument is designed for a minimum 5-year mission in High Earth orbit or, preferably, around L2. The technological solutions for ALADInO have been conceived to overcome the experimental limitations for the investigations of antimatter CRs in space with magnetic spectrometers, opening for an increase in the energy reach and in the detector acceptance, and minimizing the geomagnetic field shielding to precisely measure the GeV to supra-TeV antimatter CR components. The design of the instrument has been optimized in terms of layout, weight, dimensions, power consumption, and expected data throughput to fit in the limits set for transport and operation in Earth–Sun Lagrange Point L2 using a space vector that is already accessible nowadays. The Ariane heavy-lift launcher, also designed to transport large astrophysical instruments in L2 such as the recently launched James Webb Space Telescope [92], has been used as a benchmark opportunity for the deployment of ALADInO in L2.

Operations in space are mandatory to avoid fragmentation of primary CRs in the atmosphere before their detection and to ensure the desired observation time. Collection of CRs far from the geomagnetic field's strongest regions minimizes the disturbances and maximizes the amount of low-energy CR statistics. A time-integrated collection factor of  $\sim 15 \text{ m}^2 \text{ sr yr}$ , a MDR of at least 20 TV, and an electron/proton (e/p) separation at the level of  $10^5$  are mandatory to drive a substantial advance in the field. Velocity measurements with 1% resolution allow for  $\bar{D}$  detection in the energy range where DM signals are expected. Antimatter/matter separation with a spectrometer is not needed to study the CR spectrum at PeV energies, but a collection factor of  $\sim 20 \text{ m}^2 \text{ sr yr}$  inside the acceptance of a deep absorbing calorimeter opens the additional opportunity to measure the CR spectral composition with sufficient statistics at the highest energies.

The strategy adopted to achieve the expected performances while coping with the stringent requirements on volume, weight, power, and operations in space is based on two pillars:

- Exploit the CR isotropy with a novel detector geometry to overcome the limitations in acceptance for telescopic configurations of the spectrometers as used in PAMELA, AMS-01, and AMS-02;
- Improve the particle detection and identification capabilities with technological upgrades of well-established and reliable space qualified technologies.

A baseline design for the ALADInO detector is shown in Figure 2. The detector is equipped with a magnetic spectrometer for CR charge sign identification and rigidity measurement up to a MDR larger than 20 TV. Most importantly, only an optimized, lightweight superconducting magnet may enable overcoming the limitations of permanent magnets in space and generate the required high-intensity magnetic field. A layout based on high-temperature superconducting coils in toroidal configuration is the solution proposed in this concept. The instrument is further equipped with a 3D imaging calorimeter with high energy resolution. The calorimeter features a depth of 61 radiation lengths ( $X_0$ ) corresponding to approximately 3.5 nuclear interaction lengths ( $\lambda_I$ ) for precise measurement of the energy spectra of  $e^\pm$  and nuclei above the spectrometer MDR. Finally, the instrument is completed with a ToF featuring  $\mathcal{O}(\%)$  resolution in the velocity measurement for efficient deuteron/proton separation. The acceptance of the instrument amounts to more than  $\sim 10 \text{ m}^2 \text{ sr}$  for particles in the spectrometer acceptance and  $\sim 3 \text{ m}^2 \text{ sr}$  for particles in the calorimeter and spectrometer combined acceptance. The layout ensures a large level of cylindrical symmetry around the central axis  $z$ , which coincides with the calorimeter longitudinal axis. Figure 3 illustrates the three main acceptance configurations of the detector. The combined measurements of the spectrometer with the deep absorbing calorimeter further enables their cross-calibration, opening the opportunity for precision, data-driven determination of the absolute rigidity scale in space, improving what is achievable at calibration beams at ground and consequently reducing one of the major systematic uncer-



tainties in flux measurements [93]. Similarly, the cross-calibration improves the uncertainty on the absolute energy scale of calorimeters, which in space can be only calibrated at tens of GeV using a data-driven determination of the geomagnetic rigidity cutoff [94,95], and which strongly contributes to the error on the determination of the CR flux intensities.

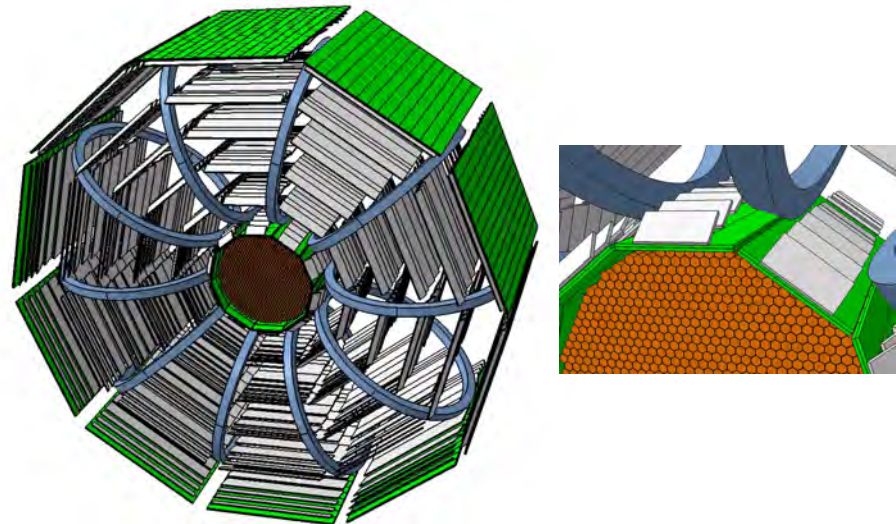


**Figure 2.** Left: Graphical rendering of the baseline design for the ALADInO detector. The core of the apparatus is a cylindrical calorimeter (orange). Ten circular magnetic coils (blue) surround the calorimeter. A silicon tracking system (gray) is arranged in six planes, each composed of several modules. Two time-of-flight planes (green), each composed of two layers of segmented scintillator paddles placed in hodoscopic configuration, are located on top of the outer tracker plane and below the innermost tracker plane. The increasing active area coverage towards the outer region of the coils minimizes the detector size and weight optimizing the combined spectrometer and calorimeter acceptance. Right: Detail of the central part of the instrument. The adaptive orientation of the tracker sensors is set to maximize the trajectory measurement resolution. Figure readapted from [96] under license CC BY 4.0.

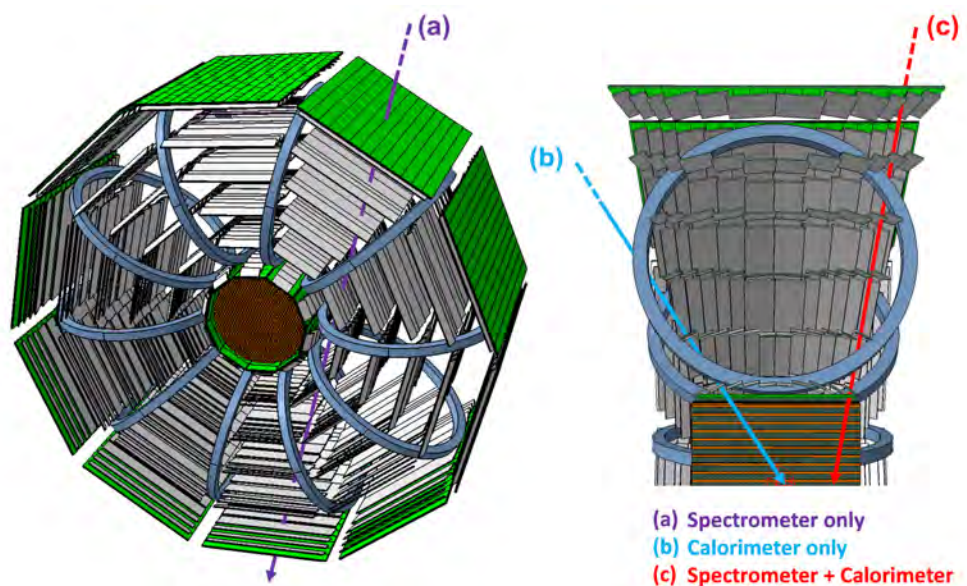


**Figure 3.** Graphical illustration of the main acceptance configurations of the ALADInO detector for high-energy particles (straight tracks). (a) Particle crossing the spectrometer only; (b) particle crossing the calorimeter only; (c) particle crossing the spectrometer and the calorimeter. Figure readapted from [96] under license CC BY 4.0.

Data transfer from ALADInO to its ground segment will be a challenge. Based on considerations on the current data production by AMS-02 [97], we expect that ALADInO will need to deliver to ground a stream of data with continuous bandwidth of  $\sim 50$  Mbps, which is in reach of what is expected, e.g., for NASA's Roman Space Telescope [98,99] planned to be operated in L2. The trigger of charged CRs will be mostly based on the fast information from the ToF. Additional fast information on energy deposit maps and tracking reconstruction from the calorimeter may be used to identify  $e^\pm$  and high-energy nuclei, for which nearly 100% efficiency should be achieved. The acquisition rate for low energy nuclei below tens of GeV must be reduced using trigger patterns with known prescaling factors: this allows for a low DAQ dead-time and to limit the data rate to be transferred to ground. Smart algorithms based on fast trajectory reconstruction inside the magnetic volume (e.g., based on Field Programmable Gate Arrays (FPGA) or Graphics Processing Unit (GPU) implementations) shall be applied to maintain a high trigger efficiency for low-energy antimatter nuclei out of the calorimeter acceptance. Random trigger prescaling will allow to estimate trigger efficiencies below 100%, thus limiting the uncertainty on the flux normalization due to the finite knowledge of the trigger response. Well-established on-board data calibration and noise suppression techniques will allow to identify the electronics channels to be recorded and transferred to ground. These approaches will enable to reach the required data size (to be determined in later phases of the planning) to further reduce the rate of data acquisition without affecting the detection of CR species which are most interesting for the physics of ALADInO. A time window of a few hours per day to transfer the ALADInO science data to ground with bandwidth of  $\sim 50$  Mbps will be enough, in reach of what is expected for the ground communication strategies of other scientific payloads operated in L2 (e.g., NASA's James Webb Space Telescope [100] and ESA's EUCLID [101]).

The most relevant ALADInO instrumental figures of merit are summarized in Table 1. Geometrical and acceptance estimations have been obtained using a simulation of the instrument detectors generated with the Generic Geant4 Simulation (GGS) package [102].

The discussion of the technological solutions to achieve the target requirements of the ALADInO detector is part of the latter section of this document.

**Table 1.** Main detector figures of merit for the baseline ALADInO mission. Values of acceptances refer to particles in the fiducial volume of the detectors [103].

ALADInO	
Spectrometer acceptance	$>10 \text{ m}^2 \text{ sr}$
Calorimeter acceptance	$9 \text{ m}^2 \text{ sr}$
Spectrometer MDR	$>20 \text{ TV}$
Combined acceptance	$3 \text{ m}^2 \text{ sr}$
Calorimeter depth	$61 X_0 - 3.5 \lambda_I$
Calorimeter energy resolution	$25\% - 35\% \text{ (h)}$ $2\% \text{ (} e^\pm \text{)}$
e/p separation	$>10^5$
Time-of-flight resolution	$<100 \text{ ps}$
Tracker spatial resolution	$<5 \mu\text{m}$
Detector weight	$<6.5 \text{ t}$
Power consumption	$\sim 3 \text{ kW}$
Readout channels	$\sim 2 \text{ M}$
Bandwidth	$\sim 50 \text{ Mbps}$
Preferred orbit	around Sun–Earth L2
Mission operation time	$>5 \text{ yr}$

### 3.1. Expected Performances for Operations of ALADInO in L2

Based on the general performances reported in Table 1, ALADInO will have the required capabilities to investigate, for the first time, unexplored frontiers of the physics

of CRs. Figures 4–6 show the expected measurements and sensitivities for the baseline ALADInO mission in a selection of relevant physics channels.

Besides the main physics channels discussed in the following, ALADInO will also have the capability to carry an unprecedented long-term campaign of nuclear CR measurements up to Fe and heavier nuclei in the supra-TeV energy range with a combined calorimetric and spectrometric approach and up to PeV energies exploiting the calorimeter-increased acceptance, and at very low energies with minimum effects by the negligible influence of the geomagnetic field in a high orbit. More details on the physics objectives of the ALADInO mission have been already discussed in detail in previous publications [96].

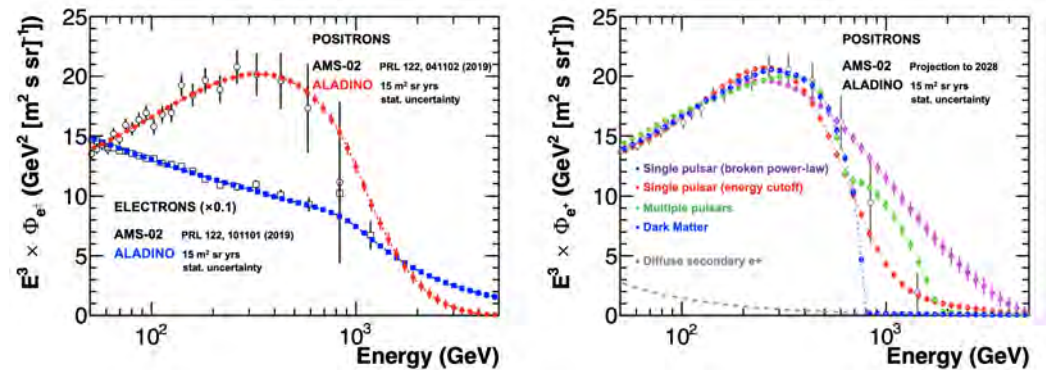


**Figure 4.** Left: Projected measurement of ALADInO after a 5-year data collection operation for the  $e^\pm$  fluxes in the descriptive model of [46,104] with a TeV break compatible with observations of [34]. Fluxes are multiplied by  $E^3$  and the  $e^-$  flux is scaled down by a factor of 10 for display purposes. Right: Projected measurement of ALADInO after a 5-year data collection operation for the  $e^+$  flux in 4 different scenarios invoking astrophysical and DM origin of high-energy  $e^+$  (violet and red from [105], green from [106], and blue from [67]) compared with the flux expected only from the  $e^+$  diffuse secondary component (gray from [46]) and with the projections for AMS-02 to 2028 [4]. The accuracy of ALADInO data in the supra-TeV region will allow to disentangle the dominating source of high-energy  $e^\pm$  and to measure directly the properties of the high-energy diffuse secondary component of  $e^+$  CRs. Figure readapted from [96] under license CC BY 4.0.

### 3.1.1. Electrons and Positrons

The most recent charge-resolved measurements of high-energy  $e^+$  and  $e^-$  are shown in Figure 4, left. Electrons and positrons show a completely different behavior above 100 GeV; in particular, the  $e^+$  spectrum shows the distinctive feature of an excess with respect to the lower energy power-law trend starting at few tens of GeV, which rises up to approximately 300 GeV and sharply drops. The available measurements are limited to a maximum reach of  $\sim 1$  TeV [46,104]. As discussed in Section 2, such properties indicate the presence of a primary, additional source of  $e^\pm$  with respect to what expected in the standard scenario of CR origin, acceleration, and propagation.

ALADInO will precisely measure the spectral behavior of the separate  $e^\pm$  fluxes above 100 GeV up to 10 TeV, accurately profiling the details of the  $e^+$  excess, maximum, and drop, and revealing for the first time the spectral features of secondary  $e^+$  from CR collisions beyond the maximum energy reach of the additional component that dominates below 1 TeV. This will open the possibility to pin down the dominating sources of primary  $e^\pm$  at high energies and possibly quantify the DM contribution to it.

The complementary high-accuracy measurement of high-energy  $e^-$  in the supra-TeV energies may allow to distinguish various contributions to the  $e^-$  and  $e^+$  energy spectra providing additional information to disentangle the origin of the high-energy  $e^\pm$  excess. Important information will be additionally provided by the measurement of the level of anisotropy (or of its upper limit) in the  $e^+$  fluxes [77,107], which will be measured with a sensitivity down to 0.2% (95% CL) above 16 GeV, corresponding to an improvement by a factor of 10 on the best limits available with the current AMS-02 experiment [46].

### 3.1.2. Antiprotons

Taking advantage of the negligible effect of geomagnetic field in its orbit, ALADInO will provide a high-statistic measurement on low-energy  $\bar{p}$  with an increase of two orders of magnitude in statistics than what is planned to be collected by the end of the AMS-02 mission [47], providing independent information to that in reach of the planned GAPS mission. ALADInO will also provide a novel, high-accuracy measurement of  $\bar{p}$  in the range up to 500 GeV, where the existing AMS-02 measurements show a tension with the astrophysical background models based on secondary production of  $\bar{p}$  from CR collisions (see, e.g., [79,80]) that no other operating or planned detectors will be able to resolve. Most importantly, ALADInO will measure for the first time the  $\bar{p}$  energy spectrum in the supra-TeV energies to provide unprecedented information on its spectral features, shedding light on an important frontier that could not be otherwise explored.

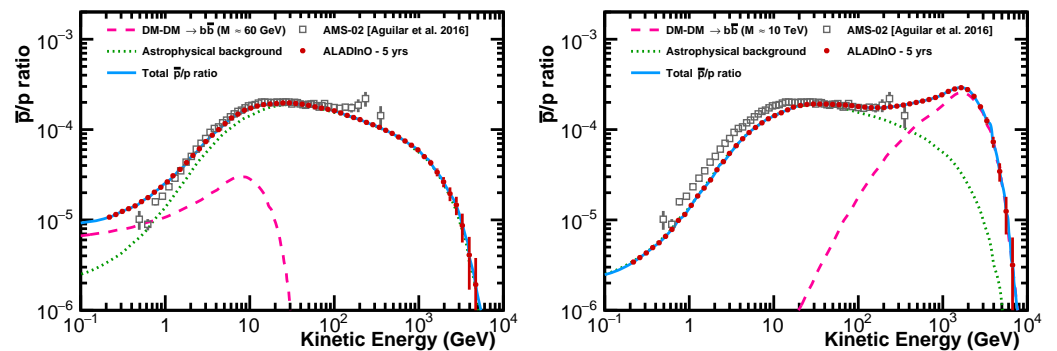


**Figure 5.** Antiproton-to-proton ratio (blue line) as a function of kinetic energy. The green dotted lines represent the contribution according to standard calculations for the astrophysical background. The two scenarios represent the contribution of an additional component from 60 GeV (left) and 10 TeV (right) mass DM particles annihilating in  $b\bar{b}$  [108] (dashed pink line). In both scenarios, projections for ALADInO in 5 years of observation time are shown (red points) and compared with the recent measurements by AMS-02 [47] (empty squares). Figure readapted from [96] under license CC BY 4.0.

### 3.1.3. Antideuteron and Antihelium

Antideuterons are considered the channel with the highest potential to provide breakthrough findings for new physics and to investigate the presence of DM in the cosmic radiation and potentially study its properties. The astrophysical  $\bar{D}$  flux in the GeV and sub-GeV energy range is extremely suppressed by kinematics, while the  $\bar{D}$  flux from DM collision is enhanced in the same region. A similar scenario is expected for the  ${}^3\text{He}$  flux, although the absolute level of intensity is strongly suppressed with respect to the  $\bar{D}$  flux [109]. Antideuteron searches are and will be performed by AMS-02 and GAPS during the coming years, with a sensitivity, respectively, of approximately  $4 \cdot 10^{-7} (\text{GeV/n})^{-1} \text{m}^{-2} \text{s}^{-1} \text{sr}^{-1}$  and of  $2 \cdot 10^{-6} (\text{GeV/n})^{-1} \text{m}^{-2} \text{s}^{-1} \text{sr}^{-1}$  [110,111] (see Appendix A for a remark on the AMS-02 sensitivity).

ALADInO will completely change the current paradigm, since the amount of collected statistics will enable not only to detect  $\bar{D}$  in CRs, but it will also open the possibility to measure its energy spectrum and spectral features up to few GeV/n, even in the case of astrophysical secondary  $\bar{D}$  contribution only (cfr. Figure 6, left).

The detection of  ${}^3\text{He}$  is instead out of reach of AMS-02 and GAPS in most of the current models, and ALADInO will represent the first opportunity for detection of  ${}^3\text{He}$  in CRs (cfr. Figure 6, right).



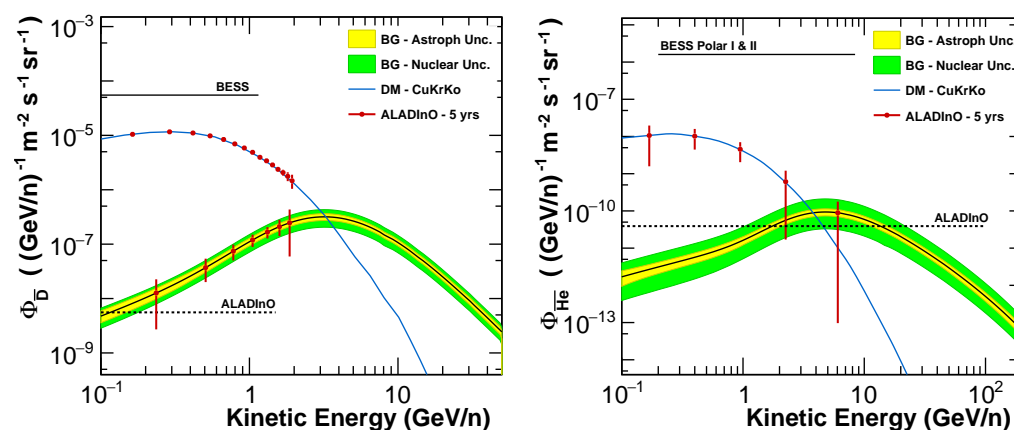


**Figure 6.** Expected measurement by ALADInO (red points) for the flux of  $\bar{D}$  (left) and  $\bar{^3\text{He}}$  (right) as a function of kinetic energy per nucleon, in the scenarios of DM models (blue lines) consistent with available antiproton data [81,112] and astrophysical background with its uncertainties [113]. The best current upper limits are also shown [114,115]. Antideuteron searches are and will be performed by AMS-02 and GAPS during the coming years. These instruments combined will leave untested a significant region of parameter space of DM models. The dotted lines show the ALADInO sensitivity level, for 5 years of exposure, over its optimal range of detection. The ALADInO measurements for the flux of  $^3\text{He}$  in case of astrophysical background only are not shown since the  $^3\text{He}$  flux would be approximately compatible with the ALADInO sensitivity. Figure readapted from [96] under license CC BY 4.0.

#### 4. ALADInO Technologies

The ALADInO subdetectors are based on well-known technologies developed for high-energy physics experiments and with high Technology Readiness Level (TRL): silicon sensors, scintillators, and homogeneous calorimeters, which have been in fact successfully operated in long-term space missions. The major challenges to enable the mission of ALADInO will be the design and operations of the superconducting magnet, the cryogenics, and thermal design of the payload; nonetheless, as discussed later in details, the established space heritages and mature ground R&D activities on the technologies that are of interest for ALADInO strongly support a scenario for a prompt start of a mission feasibility and preliminary definition (phases A and B).

As already presented in [96], the core, distinctive system of the instrument is the magnetic spectrometer. The magnetic field is generated by a superconducting toroidal magnet, composed of 10 coils that generate an average magnetic field of 0.8 T in the tracker volume, corresponding to a bending power of 1.1 T·m, while minimizing the stray field outside of the tracker volume. The usage of High-Temperature Superconductor (HTS) tapes allows to operate the magnet above 40 K, overcoming the limitations in the instrument caused by cryogenics based on liquid-He. Inside the magnetic volume, a tracking system is used to precisely measure the particle trajectory over 6 planes, which are arranged in a cylindrical adaptive configuration around the instrument axis. The measurement of the particle trajectory allows to infer the particle curvature and, thus, its rigidity and sign of the charge. The well-established silicon microstrip technology and low-noise readout electronics for precision tracking allows to reach a target spatial resolution in the bending coordinate of at least 5  $\mu\text{m}$ , with prospects to improve down to 3  $\mu\text{m}$ , with a contained power consumption of less than 2 kW for a total of  $\sim 2\text{M}$  readout channels. Together with the magnet bending power, this results in a rigidity measurement with MDR larger than 20 TV. In this configuration of the tracker planes, which feature a larger active area moving from the inner to the outer tracker layer to optimize the gathering volume of the instrument, the spectrometer acceptance is larger than 10  $\text{m}^2\text{sr}$ . A ToF system based on two concentric rings of scintillating counters at the edges of the magnet coils coupled with fast, compact Silicon Photomultipliers for light readout will provide a timing measurement



with resolution better than 100 ps, which is needed to efficiently identify the trajectory direction of particles and separate positively from negatively charged particles with the spectrometer, as well as to achieve the required velocity measurement resolution for p/D isotopical separation in the energy range where the  $\bar{D}$  signal is expected. The ALADInO instrument in its baseline configuration is completed by a large-field-of-view calorimeter placed in the center of the instrument. In order to maximize the combined spectrometer and calorimeter acceptance, the latter is designed as an array of small crystals arranged over a cylindrical volume, in an optimized geometry that maximizes the detector acceptance while minimizing the instrument weight. The calorimeter has, along its diameter, a depth of  $\sim 61 X_0$  and  $3.5 \lambda_I$ , to absorb the energy deposit of supra-TeV  $e^\pm$  and largely improve the energy resolution for deeply interacting hadrons. The 3D shower imaging capabilities allow for e/p separation based on the analysis of the shower topology that, combined with the momentum measurement by the spectrometer, results in an e/p separation capability better than  $10^5$ . The combined spectrometer and calorimeter acceptance amounts to  $3 \text{ m}^2\text{sr}$ , which allows to achieve the target statistical sensitivities for measurement of  $e^\pm$  and  $\bar{p}$  up to 10 TeV and of the nuclear CR components up to the PeV energies.

We further discuss in detail, in this document, only the baseline ALADInO layout described in this Section. Nonetheless, equipping the ALADInO instrument with additional ancillary subdetectors may enable novel capabilities and improve the performances for specific physics channels, although it should meet the limits in weight, power, and compatibility with the other main subdetectors and services. The opportunity to equip ALADInO with a Transition Radiation Detector to improve the sensitivity for  $e^\pm$  is discussed in Appendix B, and will be further investigated in the next phases of the ALADInO project.

#### 4.1. Spectrometer

To achieve the advancements in the frontier physics of CRs as discussed in Section 3, the next-generation spectrometer operated in space shall feature an average MDR larger than 20 TV over an acceptance of  $3 \text{ m}^2\text{sr}$ . The technology shall also meet the strict requirements for deployment and operation of the whole instrument in L2. In view of this, an optimized lightweight design of the spectrometer system for the ALADInO detector based on a high-intensity magnetic field generated by a superconducting magnet system in a toroidal configuration and a precision tracking system arranged in cylindrical symmetry around the toroid central axis has been investigated. The spectrometer defines the overall dimensions of the ALADInO instrument, which features a cylindrical shape with a diameter of 440 cm and 200 cm in length, and largely contributes to the power budgets of the whole instrument with a power consumption of  $\sim 1.4 \text{ kW}$  for the tracker and  $1.0 \text{ kW}$  for the cryogenics system. The average field in the tracker volume amounts to 0.8 T providing a 1.1 T·m bending power that, together with the expected bending-view coordinate resolution from the tracker, allows to achieve the required MDR for high-energy particles.

##### 4.1.1. Superconducting Magnet

The experience with magnetic spectrometers in space has been paved and established by the successful operations of the PAMELA [116] and the AMS missions (AMS-01 and later AMS-02), all equipped with permanent magnets. AMS-02 is equipped with a large dipolar permanent magnet generating 0.14 T, made of Nd-Fe-B sectors assembled in a cylindrical shell structure 0.8 m long with an inner diameter of 1.1 m [117]. The early design of AMS-02 included a superconducting magnet cooled with superfluid He, which was built and successfully tested on the ground [13,118,119] and that, few months before the launch, was replaced with a permanent magnet to overcome the limitations in the mission due to the operational constraints from liquid-He cryogenics.

The use of permanent magnets is the most reliable solution to generate magnetic fields in space because they need neither electrical supply nor control electronics and they cannot undergo failures. However, they are not viable to generate strong magnetic fields over large volumes, as required indeed to measure the supra-TeV energy frontier with a spectrometer

such as ALADInO. In addition, the structure of a magnet such as that of AMS-02 constrains the acceptance of the whole instrument to a limited angular field of view. Consequently, the generation of the magnetic field for the ALADInO instrument is provided by a superconducting toroidal magnet [120], whose preliminary design comes from the experience of the SR2S (Space Radiation Superconducting Shield) project [121,122]. A toroidal magnet allows to confine its field within the coils, leaving a faint stray field on other parts of the satellite [123]. Moreover, the resulting magnetic field has a minimized dipole moment, limiting the interactions with the environmental field (either geomagnetic or interplanetary) and, consequently, forces and torques on the spacecraft. A similar magnetic configuration was among those proposed in the past for ASTROMAG [124] and, recently, the construction of a demonstrator toroidal magnet for space spectrometers was proposed in the framework of a collaboration between CERN and Italian Space Agency [125].

The ALADInO toroid is composed by 10 coils, a number chosen as the best compromise between two requirements: to maximize the magnetic field azimuthal homogeneity, which needs distributed conductors (large number of coils), and to maximize the field of view, which requires concentrated conductors (small number of coils). The coils composing a toroid can have several shapes (e.g., round, racetrack, D-shaped) with different benefits and drawbacks, and the shape will be determined to optimize the overall detector performances. Figure 7 shows the magnet and the map of the magnetic field in a configuration with 10 round coils with 1.45 m diameter. Since the toroid hosts the calorimeter inside its inner bore, the minimum inner diameter is set to 1 m and the overall magnet radial dimension is approximately 4.3 m. With  $440 \cdot 10^3$  ampere-turns per coil, the average field on the tracker is 0.8 T and the stored energy amounts to 3.6 MJ. The maximum field at the conductor is limited to 3 T. In this configuration of the magnet, the magnetic field is mostly uniform in the azimuthal direction defined by the coil system. Most importantly, this configuration of the magnetic field allows to equip the tracking system with position-sensitive sensors featuring high resolution for measurement of the particle bending direction and lower resolution for the perpendicular direction, mitigating the power requirements and the complexity of the system.

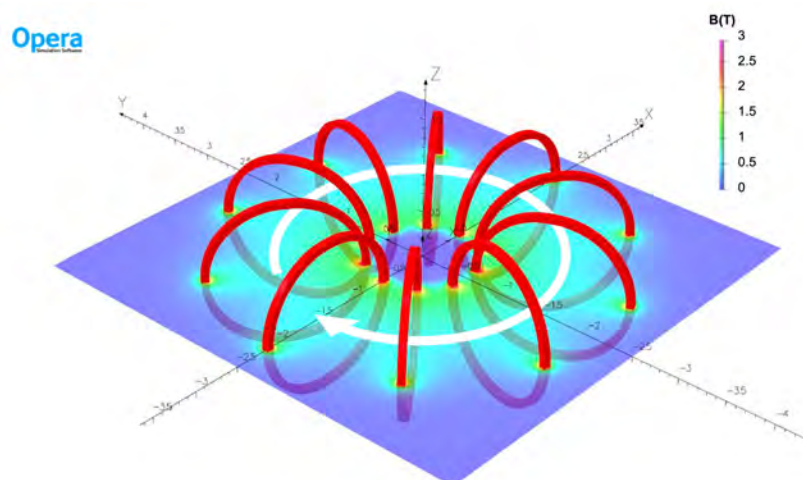


**Figure 7.** Schematic rendering of the magnet and map of the generated magnetic field in the configuration of 10 round coils with the geometry discussed in the text. The field has been simulated using [126]. The white arrow sketches the direction of the magnetic field inside the coils. Figure readapted from [96] under license CC BY 4.0.

The coils will be wound with tapes based on HTS, specifically, ReBCO (Rare Earths Barium Copper Oxide) tapes. Such a conductor allows to operate the magnet at temperatures up to 40 K, avoiding liquid-He cryogenics and the consequent limitations for long-term stable operations in space. High operative temperatures also provides large robustness against quench-trigger disturbances. These are related to the specific heat ca-

capacity at 40 K of solid materials, which is two orders of magnitude higher with respect to the corresponding values at 4.2 K. This dramatically increases the enthalpy margin of the magnet. Consequently, the Minimum Quenching Energy (MQE) is so high that the energy releases sufficient to initiate quenches in low-temperature magnets do not affect the operations of a ReBCO magnet. The extremely high stability of HTS magnets operating at 40 K, indeed, limits the possible causes of quenches due to failures of the cryogenic system or to dreadful events such as debris impact.

Although unlikely, quench protection should be considered and is known to be a major issue in HTS magnets. A possible solution, which does not require any active quench protection system, is the no-insulation (NI) technique [127] (actually, a resistive metal insulation) which, in case of quench, allows for current diffusion and protects the coils. Of course, the lack of dielectric insulation affects the charging ramp rate, which must be adjusted according to the magnet time constant (up to order of tens of hours). A problem associated with no-insulation winding in a toroidal magnet in case of quench or fast discharge is the generation of forces and torques between the coils that must be supported by a suitable mechanical structure.

State-of-the-art, 4 mm wide, 0.1 mm thick, ReBCO conductors have critical current  $I_c$  (3 T, 40 K)  $> 300$  A [128]. Therefore, the operative current can be set to 244 A, maintaining an acceptable margin. The number of turns will be 1800/coil and the magnet inductance about 120 H. Further developments in conductor performances can lead to the reduction of the number of turns. In the described configuration, the mass of the conductor amounts to approximately 900 kg. The mass of the magnet, including the mechanical structure, is estimated to be approximately 1200 kg [120]. The main characteristics of the magnet proposed for ALADInO are shown in Table 2.

**Table 2.** Main characteristics of the superconducting magnet based on HTS ReBCO tapes proposed for ALADInO.

Superconducting Magnet	
Number of coils	10
Total current per coil	$440 \cdot 10^3$ A
Operating current	244 A
Inductance	120 H
Average magnetic flux density	0.8 T
Bending power	1.1 T·m
Cold mass	1200 kg

To minimize the heat load and most efficiently operate the magnet in space, the magnet is planned to be operated in persistent mode [120], similarly to those used for medical Magnetic Resonance Imaging (MRI). In persistent operation mode, two methods are possible to charge the magnet: a power supply with disconnectable current leads or a flux pump. Considering that the magnet must be charged very slowly, the flux pump is an attractive solution that avoids moving parts and limits the size of the power supply. Operations of the magnet in persistent mode require high inductance and low resistance. In a magnet operating far from the critical current, resistance mainly comes from joints. Methods to make superconducting joints between ReBCO tapes have been proposed [129] and the technology is quickly developing, leading to great confidence that such solution could be available at the magnet construction time. Nonetheless, in case soldered resistive joints must be used, the flux pump can compensate the current decrease that, supposing  $1 \mu\Omega$  total resistance, is limited to about 2% per month.

Cryogenics is an important aspect in designing a space magnet that integrates a particle detector. The heat load on superconducting systems comes from three main sources: the external environment (mainly the Sun), the calorimeter, and the other detectors (ToF and tracker). In principle, passive cooling could be a viable solution, taking advantage of the low temperature of deep space. However, it would require large area radiators.

The use of cryocoolers consequently appears as a preferable choice. The thermal radiation power coming from the several sources will be intercepted by a series of radiation shields. A passive multilayer, umbrella-like, sunshield will be used to intercept the radiation heat flux from Sun [130]. The sunshield technology is the same used for the Planck satellite [131] and the James Webb Space Telescope [132,133].

The superconducting coils are subject to multidirectional thermal radiation from the calorimeter, ToF sunshield and tracker, which are supposed to be operated at high temperatures. While current spectrometers in space have been operated with temperatures of their subdetectors around 250 K, studies are in progress to verify the minimum working temperature of the detector components and, consequently, decrease the heat load on the magnet. Two thermal shield systems plus cryogenic Multilayer Insulation (MLI) will be placed around each coil. The first shield set, directly facing the 250 K surfaces, will be actively maintained at about 80 K by a cryocooler, while the second one, thermally passive, will be at a temperature close to the magnet working temperature. The 80 K shields will be thermally connected to the cryocooler by nitrogen pulsating heat pipes, which are much lighter and efficient than pure copper straps [134–137]. The supports and tie-rods connecting the coils to the external structure at 250 K will be made using high-strength, low-thermal-conductivity, materials such as G-10 glass-fiber/epoxy composite. The heat load is estimated to be in the order of 60 W at 80 K and 3 W at 40 K [120].

In order to reach the TRL of technologies to enable the properties of the superconducting magnet described in this document for the design proposed for ALADInO, we expect, as of today, contained R&D technological activities beyond the state of the art, reasonably lasting 5–6 years. Considering an additional 5 years for design, construction, tests, and integration, the superconducting magnet for ALADInO could be ready for operations in space within approximately 10 years.

#### 4.1.2. Tracker

Tracking with a  $\mathcal{O}(\mu\text{m})$  coordinate resolution is achieved in ALADInO, in its baseline design, using double-sided silicon microstrip detectors. While originally developed in the 1980s for microvertex detectors in High-Energy Physics experiments at colliders, the precursor flight of the AMS experiment on the STS-91 mission of the Shuttle Discovery in 1998 first demonstrated that thin  $\mathcal{O}(300\ \mu\text{m})$  silicon microstrip detectors can be successfully operated for precision particle tracking in space. Since then, silicon trackers have been adopted in most space-borne calorimetric experiments (AGILE [138], Fermi-LAT [139], DAMPE [140]), or magnetic spectrometers (PAMELA [29], AMS-01 [28], AMS-02 [30]), for cosmic ray and gamma-ray measurements in space. As of today,  $\mathcal{O}(100\ \text{m}^2)$  of silicon sensors for tracking detectors are currently being operated successfully in space in long-term missions.

In silicon microstrip trackers, precision measurement of particle coordinates is accomplished by lightweight, thin layers of active material along the particle trajectory, consequently reducing the amount of multiple scattering throughout the particle trajectory. Moreover, silicon microstrip trackers can be operated in absence of consumables (contrary to gas detectors) and relatively low voltages (few tens of V for sensors with thickness of hundreds  $\mu\text{m}$ ). The position of the particle is determined by the analysis of the signal amplitudes detected by the readout strips closest to the particle crossing trajectory, whereas the particle charge magnitude can be assessed from the amplitude of the total energy deposit in silicon, which is proportional to  $Z^2$ , readout by high-dynamic-range front-end electronics (FEE) [30].

The design of the tracking system proposed for ALADInO takes advantage from the heritage of the AMS and PAMELA experiments. In its baseline design, it is composed of 7540 high-resistivity silicon microstrip sensors,  $95 \times 95\ \text{mm}^2$  each, for a total detector surface of about  $68\ \text{m}^2$ . The sensor design exploits capacitive charge coupling with floating strips to achieve optimal spatial resolution with a reduced number of readout channels [141]. Sensors are planned to feature, for the bending (nonbending) direction, an implant strip



pitch of  $\sim 25\ \mu\text{m}$  ( $\sim 32.5\ \mu\text{m}$  or  $\sim 75\ \mu\text{m}$ ) and a readout pitch of  $\sim 100\ \mu\text{m}$  ( $\sim 150\ \mu\text{m}$  or  $\sim 300\ \mu\text{m}$ ), thus reading out only one every 4 strips.

The silicon sensors are grouped together for readout and biasing into ladders, each composed of a variable number of sensors (2 to 7 sensors per ladder, for a total ladder length up to 66.5 cm) to match the size of the different tracker planes. To minimize the material in the tracking volume, the FEE is located at the ladder ends. Strips parallel to the magnetic field lines are daisy-chained through direct microbondings between adjacent sensors. Exploiting the solution already used, e.g., for the AMS-02 tracker, a metalized Upilex film running over the ladder length is used for coupling transversal strips to the corresponding FEE located at the longitudinal edge of the ladder. Each ladder will be connected to 15 (10) readout chips, 64 channels each, for a total of 960 (640) readout channels in the bending (nonbending) direction, with an estimated power consumption of  $\sim 0.5\ \text{W}$  per ladder. To provide a possible visualization of ladder units planned for ALADInO, Figure 8 shows, as reference, the two sides of a ladder built for the AMS-02 detector using smaller ( $40 \times 70\ \text{mm}^2$ ) silicon sensors.



**Figure 8.** Picture of an AMS-02 ladder made of 12 double-sided  $40 \times 70\ \text{mm}^2$  silicon microstrip sensors, enclosed in a plastic transport box. Strips measuring the bending direction are readout using a daisy-chain microbonding connection (top view), while transversal strips are readout via additional routing provided by a metalized Upilex film (bottom view), such that the FEE readout is located at the longitudinal edge of the ladder.

The ALADInO tracker is designed to be made of a total of  $\sim 1400$  ladders arranged over six planes surrounding the calorimeter, as visible in Figure 2. The tracker ladders will be mounted on mechanical support planes made of a low-density aluminum honeycomb structure enclosed within thin Carbon Fiber Reinforced Polymer (CFRP) skin. In order to fully exploit the intrinsic resolution of the detectors, and given the worsening of the resolution for very inclined tracks, a peculiar ladder orientation has been devised, as shown in Figure 9. The tracker is composed of 10 sections, each hosting 6 tracker planes between the inner and outer ToF units (see Section 4.3 for the ToF system description), with increasing active area coverage towards the outer region of the coils to minimize the detector size and weight while optimizing the combined spectrometer and calorimeter acceptance. Each section of the ALADInO tracker roughly corresponds in terms of number of sensors, number of readout channels, and amount in silicon microstrip area, to the whole AMS-02 tracker. The exploitation of the AMS-02 heritage, consequently, strongly supports the need of a contained R&D activity to enable the construction of the ALADInO tracker.



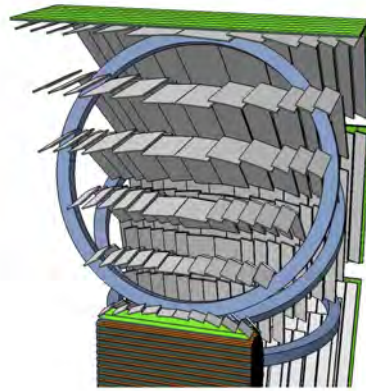


**Figure 9.** Detailed rendering of the silicon ladder orientation in the ALADInO tracker, optimized to reduce the occurrence of particles with large incident angles in the tracker sensor acceptance. Figure readapted from [96] under license CC BY 4.0.

The sensor readout pitch, together with low-noise FEE, will ensure a position resolution more accurate than  $5\ \mu\text{m}$  for vertically crossing particles. Better performances have already been obtained by the PAMELA collaboration using shorter ladders but with a very similar implant pitch [142] (see Figure 10, left). The AMS-02 collaboration has instead demonstrated the possibility to use long detector modules (up to 60 cm, similar to the 66.5 cm length planned for ALADInO), obtaining a resolution better than  $10\ \mu\text{m}$  ( $5\text{--}8\ \mu\text{m}$ ) for  $Z = 1$  ( $Z > 1$ ) particles [143]. Further taking advantage of this heritage, negligible R&D is expected towards the implementation of the ALADInO tracker.

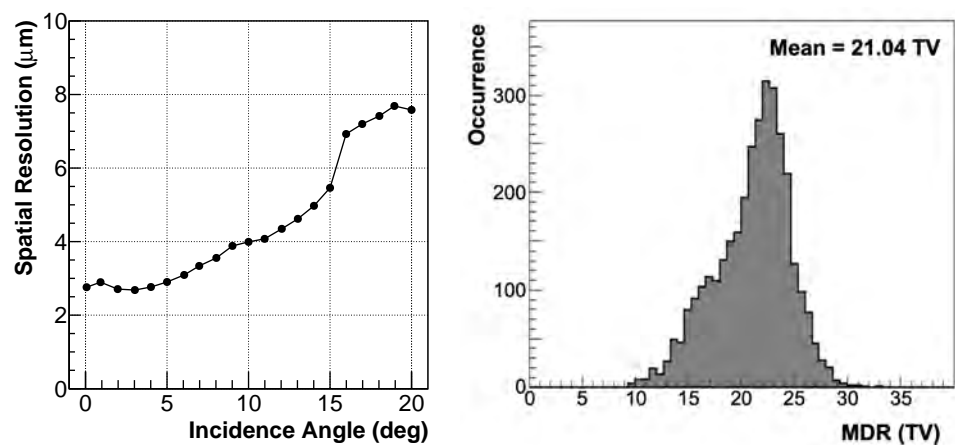


**Figure 10.** Left: Spatial resolution of the PAMELA tracker short ladders as a function of the particle incident angle. Figure recreated by authors of [142] from original data files, see original paper for details. Right: Distribution of the MDR of the ALADInO spectrometer evaluated with preliminary numerical simulations over a wide range of incident angles. The result confirms the reach of an average MDR larger than 20 TV for the expected tracker coordinate resolution.

To reach the aforementioned coordinate resolutions, an excellent knowledge of the sensor positions must be achieved. The procedure is called, in jargon, alignment. After a preliminary sensor alignment using cosmic muons or test beam particles at ground [30], sensors will be subject to misplacement during transport, installation, and operations in space. Based on the experience with PAMELA [29] and AMS-02 [4,144], a sensor alignment down to few  $\mu\text{m}$  can be reached using high-energy proton and He tracks. Any residual systematic misalignment (i.e., “coherent misalignment”, introduced by the alignment procedures that are performed using particles with positive charge only) can be solved by

corrections from the comparison of  $e^+$  and  $e^-$  rigidity measurements to the energy measurements by the calorimeter [93]. The ALADInO tracker will operate in an environment different than that of PAMELA and AMS-02, inside a superconducting and more intense magnet and in a peculiar but more stable thermal environment. In view of this, extensive simulations and tests at ground will be carried out to define the most proper strategy to achieve the sensor position accuracy required to reach the target rigidity measurement resolution. Finally, unprecedented approaches may come from the possibility to switch off the magnetic field and align the tracker using undeflected tracks: this represents a very powerful opportunity to improve the tracker alignment, whose technical feasibility will be an objective of dedicated studies in the advanced phase of the detector design.

The benchmark for power consumption of FEE readout of currently operating microstrip silicon detectors amounts to 0.3 mW per channel, such as that of the DAMPE tracker [140], which adopts an improved version [145] of the same FEE used for PAMELA and AMS-02. With a moderate R&D activity mostly aimed at the optimization of the readout FEE, it is consequently conceivable to obtain the design value of  $\sim 3 \mu\text{m}$  coordinate resolution on long detector modules planned for ALADInO while keeping the aforementioned limited power consumption.

The dynamic range of the FEE shall extend to reach at least the Oxygen ( $Z = 8$ ) signal amplitude without saturation, as already done for AMS-02 [146]. For  $Z > 8$ , in fact, if the strip closest to the particle impact point in the sensor is saturated, the charge coupling between adjacent strips will allow to recover the charge measurement. The expected charge measurement resolution combining the 6 tracker plane measurements is expected to be better than 0.15 c.u. (charge units) for  $Z < 10$  and better than 0.3 c.u. for  $Z$  up to 26 (Iron) and above.

In its baseline configuration, the silicon tracker of ALADInO is expected to have a total power consumption, for the FEE, of approximately 700 W. Based on the experience gained in the design and implementation of the current and past generation of silicon trackers in space, the Data Acquisition (DAQ) system reading the FEE is expected to consume an additional  $\sim 750$  W. Differently from the FEE, the DAQ device is planned to be located at the periphery of the apparatus far away from the sensors and it will not strongly contribute to the heat load to be dissipated from inside the spectrometer volume.

The expected performances of the ALADInO tracker have been evaluated using numeric simulations and track fitting algorithms of particle tracking in the benchmark magnetic configuration described in Section 4.1.1 for different conditions of pitch angles. Preliminary results are shown in Figure 10, right, which provides the confirmation that with the design magnetic field, tracker geometry, and coordinate measurement resolution, the MDR of the spectrometer is of the order of 20 TV.

#### 4.1.3. Possible Improvements of the ALADInO Tracker

In a time frame relevant for the project, emerging technologies could become mature enough to be evaluated as replacement for the silicon microstrip technology planned for the benchmark design. We discuss the possibility to adopt new technologies that may provide improved performances and capabilities to the ALADInO tracker.

##### Timing Layers

Low-Gain Avalanche Diodes (LGAD), also called Ultra-Fast Silicon Detectors (UFSD) [147], are silicon sensors that feature thinner layers (i.e., less material budget) with the same, or even higher, signal/noise electronic level, which could be considered to replace standard microstrip Si sensors. The LGAD technology may provide the ALADInO tracker with timing capabilities in addition to the precision coordinate measurement, with performances similar to those of the plastic scintillator ToF (i.e., resolutions  $< 100$  ps), providing the apparatus with an independent time-of-flight detector to improve the overall performances (e.g., nuclear isotopical separation) and give further redundancy to cross-calibrate the detectors. Timing information in the tracker could be measured with a spatial granularity down to

$\mathcal{O}(1\text{ cm}^2)$  (as opposed to the  $\mathcal{O}(100\text{ cm}^2)$  of the plastic scintillator ToF), opening the opportunity for a combined trajectory and timing measurement at the level of single particle even in the harsh environment of high hit occupancy in the tracker due to large back-scattering from the calorimeter. The timing capability will thus allow to identify energy deposits in the tracking planes due to back-scattering particles from the calorimeter and to pile-up from cosmic rays (i.e., two primary cosmic rays impinging the detector inside the same trigger and FEE sampling time window), consequently improving the overall tracking reconstruction efficiency and identification capabilities of the apparatus [148].

In order to enable the readout of the coordinate and timing information over the  $\sim 2\text{ M}$  tracker channels, dedicated R&D activity is required, mostly for the development of a low-power consumption Application Specific Integrated Circuit (ASIC) for the concurrent time and coordinate readout of LGAD sensors, as well as power-consumption mitigation approaches in the signal readout strategy. In the state of art, silicon microstrip FEE used in physics instrumentation (e.g., [145]) feature a power consumption of  $0.3\text{ mW/channel}$ . Commercially available front-end chips for Silicon Photomultiplier readout (e.g., [149]) feature few tens of ps resolution with  $6\text{ mW/channel}$  power consumption. Since the signal amplitude produced by a Silicon Photomultiplier in the case of a single photon avalanche is similar to that produced by a charged particle crossing a typical UFSD with a inner avalanche layer with a gain of the order of 10, such consumption could be considered as an available benchmark. It is likely to envisage in the time frame relevant for the project a reduction in the power consumption per channel from developments in the technology of such devices or from the optimization of a custom ASIC designed specifically for LGAD microstrip sensors to be operated in space. Scaling down the consumption by a reasonable factor  $\sim 2$  would result in a total tracker power consumption of  $\sim 5\text{ kW}$ , which is expected to be compatible for operations of the tracker in space.

A possible backup solution to reduce the power consumption and meet the requirement of an overall  $\sim 5\text{ kW}$  power budget while keeping the current benchmark consumption per channel could also involve reading out one every two strips and taking advantage of the capacitive charge sharing to measure the timing for most of tracks, or even group separate strips with a unique FEE timing channel while keeping separate strip FEE readout for charge/position measurement. This is not expected to significantly degrade the particle identification capabilities offered by the combined timing and coordinate measurement itself.

#### Pixel Technology Monolithic Active Pixel Sensors

Particle trajectories can be also tracked with Monolithic Active Pixel Sensors (MAPS [150]). MAPS feature in-pixel front-end electronics, with significant gain in terms of signal-to-noise ratio. Data management is carried out on the periphery of the sensor, with in situ zero-suppression and encoding allowing unequaled data throughput [151]. This feature is particularly important in dense environments, e.g., near or inside the calorimeters, providing high-resolution imaging capabilities besides single-hit measurements.

Currently available MAPS are as large as few  $\text{cm}^2$ , with 95% active area. They can be thinned down to  $50\text{ }\mu\text{m}$ , reducing the impact of the material on the trajectory of the particle to less than any other silicon-based option [152,153]. Pixel sides as large as  $25\text{ }\mu\text{m}$  are routinely implemented, allowing for single-hit resolution as low as  $4\text{ }\mu\text{m}$  after corrections for charge diffusion. These figures are rapidly improving, with next-generation MAPS prototypes as large as  $\sim 20\text{ cm}^2$ , pixel side as low as  $10\text{ }\mu\text{m}$ , and thickness reduced to  $35\text{ }\mu\text{m}$  [154].

One- and two-dimensional stitching techniques proved to be effective for adaptation of MAPS to complex and inhomogeneous mechanical supports: bent and tilted solutions allow to limit the regions with increased material thickness opposed to the particle motion. MAPS are fabricated with Complementary metal-oxide-semiconductor (CMOS) technologies, sharing large-scale fabrication processes and infrastructures with image sensors.

Shared platforms and test benches allow for a swift pace of development and a remarkable containment of costs.

At the time of writing, power consumption as low as  $20 \text{ mW/cm}^2$  has been measured for payloads on instrumented areas as large as hundreds of  $\text{cm}^2$ . Prototypes of next-generation Fully Depleted MAPS are available with power consumption reduced to  $5 \text{ mW/cm}^2$  for squared pixel layouts and  $<1 \text{ mW/cm}^2$  for striplike sensing elements (typical dimensions of  $25 \mu\text{m} \times 500 \mu\text{m}$ ) [155]. A striplike geometry is particularly relevant for an application where different spatial resolutions are required—for example, in ALADInO—to measure bending and nonbending coordinates.

A number of features of MAPS are already used to further reduce power consumption. For instance, analog front-end and discriminator can be continuously active allowing to power the digital readout only for regions of interest for data acquisition. MAPS fabricated with CMOS  $180 \mu\text{m}$  technology have been chosen for the HEPD-02 payload, to be launched on-board the CSES-02 satellite by the end of 2022 [156,157]. Further heritage comes from Timepix hybrid pixel detectors [158], successfully used for dosimetry in space.

#### 4.2. Calorimeter

The main objective of the ALADInO calorimeter is to provide independent and complementary measurements to those of the spectrometer in order to reach the required accuracy for measurement of antimatter and high-energy CRs. In particular, the ALADInO calorimeter has been designed to be operated at the center of the spectrometer coils to:

- Ensure a nearly isotropic response to particles entering from different directions, thus maximizing the detector acceptance;
- Provide a 3D imaging reconstruction of the shower topology to accurately measure the energy of the primary CR for both electromagnetic and hadronic showers and to efficiently separate between electron- and hadron-initiated showers.

The design of the ALADInO calorimeter is based on the CaloCube R&D project [159–161], which, for the first time, has paved the way for the optimization of a calorimeter concept specifically designed for the measurement of particles impinging isotropically on the calorimeter. This concept well fits with the geometry of the ALADInO spectrometer. In addition, its development will benefit from the experience gained in the design, preliminary tests, and possible future commissioning of the HERD calorimeter [31,162].

The cylindrical ALADInO calorimeter is made of a 3D mesh of small hexagonal, prism-shaped, scintillating crystals. The highly segmented design allows to efficiently reconstruct the shower development inside the calorimeter independently on the incoming particle direction and to provide the required e/p separation by the 3D sampling of the shower development topology. The calorimeter crystals are made of Cerium-doped Lutetium Yttrium Orthosilicate (LYSO). LYSO is a dense and bright inorganic scintillator, nowadays easily commercially procurable. Its density ( $\rho = 7.4 \text{ g/cm}^3$ ), radiation length ( $X_0 = 1.14 \text{ cm}$ ), Molière radius ( $R_M = 2.07 \text{ cm}$ ), nuclear interaction length ( $\lambda_I = 20.9 \text{ cm}$ ), and refractive index ( $n = 1.82$ ) make it a competitive material for compact calorimeters. Its emission is centered at  $\sim 430 \text{ nm}$ , with a decay time constant of  $40 \text{ ns}$ . It is rather insensitive to temperature changes (with a relative light-yield temperature dependence of  $dLy/dT [20^\circ\text{C}] = -0.2\%/^\circ\text{C}$ ) and, thus, suitable for high-precision calorimetry in the harsh space environment [163]. In view of its properties, LYSO provides better performances with respect to other scintillating crystal materials, especially for nuclei measurements, as consequence of its larger interaction probability and larger shower containment (see, e.g., [159] for a comparative performance study on several crystal materials). In view of this, LYSO has been selected as the benchmark solution for calorimetric measurements in operating and planned small- and large-size missions (such as, e.g., [162,164,165]).

The cylindrical shape and dimensions of the active volume of the proposed calorimeter design are shown in Figure 11. The calorimeter is arranged in 637 lines each composed of 25 scintillating crystals resulting in a total 3D mesh of 15925 crystals. Each crystal is shaped as  $3 \text{ cm}$  side regular hexagonal prism. Crystals are homogeneously arranged in

the calorimeter array matrix to completely avoid escape planes, i.e., particle trajectories completely traversing the calorimeter between gaps. This approach limits the worsening of energy resolution due to the narrow lateral topology of the electromagnetic shower component, for which the presence of escape planes increases the event-by-event fluctuations in the total energy deposit. In this configuration, relatively large gaps of 8 mm are left between crystals to increase the total calorimeter acceptance without a significant loss in energy resolution. Figure 12 sketches the design of the hexagonal prism crystals and the arrangement of the crystals in the array in an optimized honeycomb geometry. The figure also shows the design of two adjacent strings of 25 assembled crystal prisms: along the longitudinal axis of the calorimeter, crystals are staggered by half-length to avoid dead space. Figure 13 shows the front view of the calorimeter placed in the center of the ALADInO experiment.

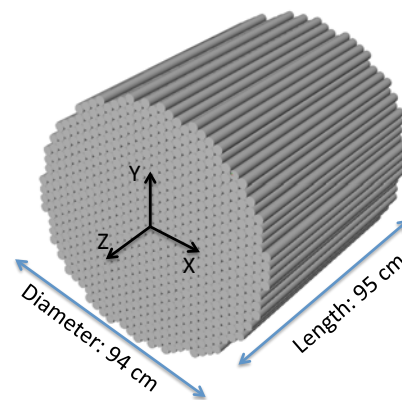


**Figure 11.** Representation of the active volume of the ALADInO calorimeter. 15925 LYSO crystals are arranged in a total assembly of 637 lines, each made of 25 aligned hexagonal prism crystals. Figure readapted from [96] under license CC BY 4.0.

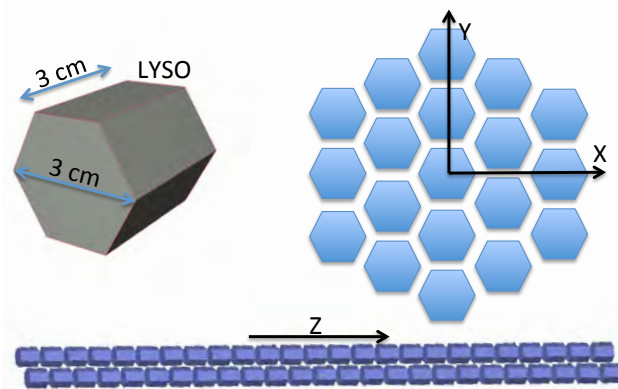


**Figure 12.** Top left: rendering of the LYSO crystal hexagonal prism shape. Top right: placement of LYSO crystals in the honeycomb layout projected on the X–Y plane. A gap up to 8 mm between crystals has been used as optimal compromise to maximize the detector acceptance while keeping a limited mass budget and without largely impacting the energy resolution for laterally narrow showers. Bottom: placement of LYSO crystals along the longitudinal axis of the calorimeter. Crystals with the same X coordinate are staggered by half-length to avoid dead spaces. Figure readapted from [96] under license CC BY 4.0.



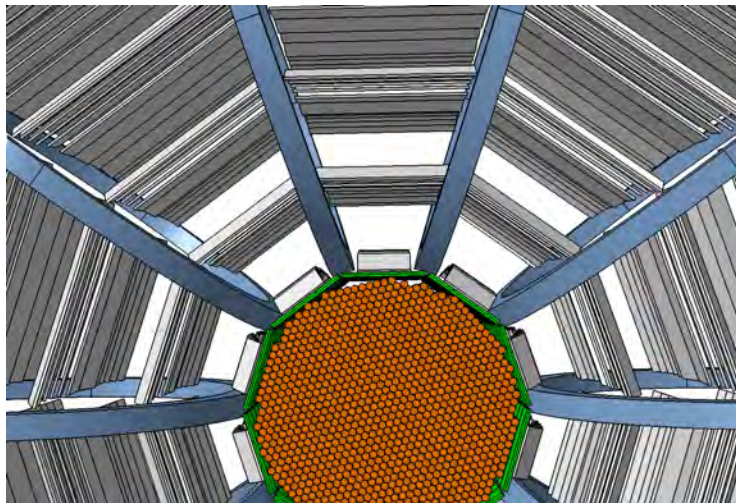


**Figure 13.** Detailed rendering of the front view of the ALADInO calorimeter (orange) placed in the center of the apparatus.

The chosen geometry is the most effective compromise between a fully isotropic calorimeter (i.e., a sphere with uniform response to particles over its entire surface) and the technical requirements on crystal procurement, uniform volume coverage, and on the deployment of electronics/mechanical structures and services for the payload. Besides the maximization of the detector acceptance while keeping equal mass, the 8 mm gaps between adjacent crystals allows to accommodate support structures and readout elements.

The calorimeter depth along the diameter corresponds to  $3.5 \lambda_I$  and to  $61 X_0$ , with a corresponding  $\sim 9 \text{ m}^2 \text{ sr}$  geometric factor for the lateral surface. Its total weight amounts to approximately 2000 kg.

The signals in the calorimeter crystals are expected to vary from  $\sim 30 \text{ MeV}$  released by Minimum Ionizing Particles (MIP), i.e., relativistic protons not interacting in the detector, to the  $10^7$  MIP signal released in one single crystal by a PeV-interacting hadron. A correspondingly wide dynamic range is then required for the readout FEE to allow for signal calibration and avoid electronics saturation for high-energy deposits in single crystals.

The light produced in the calorimeter crystals can be measured by photodiodes glued directly on the surface of each crystal. Two different photodiodes coupled to a large dynamic range FEE, one with a large collecting area for low signal intensities and one with smaller collecting area for high intensity signals, will be used to match the required dynamic range. The application of an optical filter with low transmittance to the small-area detector could provide further extension of the dynamic range. This approach has been investigated and already tested in the development of the HERD photodiode readout [162]. An alternative solution that uses wavelength shifting fiber bundles coupled to the faces of the crystals to route the light signals to photosensors placed outside the active volume of the calorimeter is also being investigated [31,162]. This approach avoids the occurrence of ionization signals directly produced by particles of the showers traversing the photodiode inside the calorimeter.

Benefiting on the already gained experience on the HERD calorimeter [162], the R&D phase and the effort to reach the required calorimeter performances is expected to be limited. The development of the photodiode readout using a pair of sensors with different areas for extension of the dynamic range for the HERD calorimeter also provides a relevant heritage for concept, development, and tests. The natural starting choice for the FEE would be to use the HIDRA chip [166], developed by INFN for space experiments. It features low noise (about 2500 electrons), low power consumption (2.8 mW/channel), and large dynamic range (from few fC to  $\sim 50 \text{ pC}$ ). In this ASIC, the dynamic range is obtained using a charge-sensitive amplifier with an automatic double-gain selection and a correlated double sampling circuit with a gain ratio of approximately 20. The expected

saturation level for the small-size photodiode amounts to hundreds of TeV, which is enough to measure PeV hadronic showers without sizable degradation of the calorimeter performances. The possible overlap of signal between the two photodiodes allows for data-driven energy scale calibration. Using the HIDRA chip performances as a reference, the total power consumption of the FEE and DAQ for the ALADInO calorimeter is expected to be approximately 200 W, with potential to be improved within the timeframe of the project.

The calorimeter performances have been studied using numerical MonteCarlo simulations based on FLUKA [167] that fully implement the calorimeter geometry, including the carbon fiber support structure between crystals. Fluxes of electrons and protons in a wide energy range have been simulated impinging isotropically on the calorimeter cylindrical surface. The shower reconstruction algorithm takes advantage of the 3D segmentation of the calorimeter to identify the first point of hard nuclear interaction and consequently estimate the length of the shower inside the calorimeter, regardless of the position and arrival direction of the incoming particle. The energy resolution for electrons and positrons has been evaluated, also with beam test experimental data for the CaloCube prototype [168], to be better than 2% above few hundreds GeV. The finite interaction length of the calorimeter limits the energy resolution for hadrons to around 30%, depending on the amount of traversed material. Figure 14 shows the shower length distribution for 1 TeV protons after an event selection aimed to have a reliable energy measurement that operates on the calorimeter fiducial volume and on the particle pathlength inside the crystals. Based on this selection, an effective geometric factor has been defined as the overall geometrical factor multiplied by the selection efficiency. For 1 TeV protons impinging isotropically on the calorimeter, the effective geometric factor of the calorimeter can reach  $5 \text{ m}^2 \text{ sr}$ , with an energy resolution varying between 24% at  $1 \text{ m}^2 \text{ sr}$  to 35% at  $5 \text{ m}^2 \text{ sr}$ . Simulations studies on large acceptance calorimeters for CR detection in space show that the energy resolution is largely independent on the value of the primary particle energy up to 1 PeV, and improves for higher charge nuclei due to their reduced interaction length and lower intrinsic shower fluctuations [159].

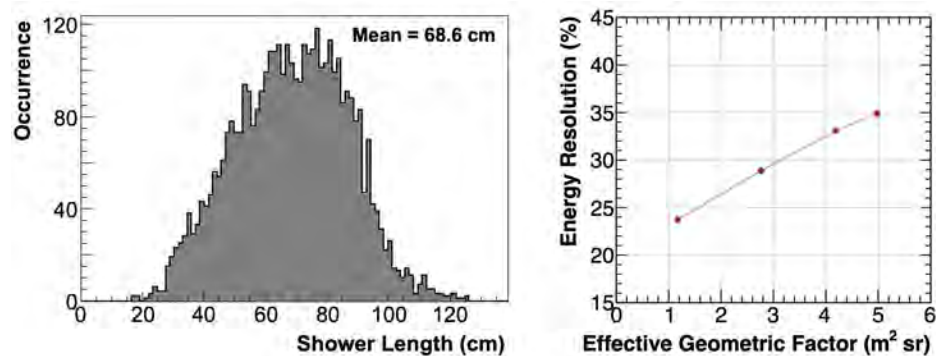


**Figure 14.** Left: distribution of the shower length in the calorimeter after the point of first hadronic interaction for 1 TeV protons impinging isotropically on the calorimeter. Right: dependence of the energy resolution for 1 TeV protons as a function of the effective geometric factor defined by a selection on the calorimeter fiducial volume and on the particle pathlength inside the calorimeter crystals.

The 3D imaging capability of the calorimeter allows to separate between positron-initiated and proton-initiated showers, which is a feature required for the measurement of the  $e^\pm$  components in CRs. Considering that the proton flux in the TeV energy range is several orders of magnitude ( $10^3$ – $10^4$ ) higher than the positron flux, an  $e/p$  separation factor of at least  $10^5$  is needed. Proton-initiated showers develop more deeply in the calorimeter and their lateral spread is larger than positron-initiated showers. Moreover, positrons are expected to deposit most of their energy in the calorimeter, while protons deposit only a fraction of their energy in the calorimeter. The comparison between the energy deposit in the calorimeter and the rigidity measurement by the tracker provides

additional e/p separation capabilities to the whole detector. In the framework of the CaloCube project [159,161,168] preliminary simulations of the proton rejection capabilities for a similar calorimeter composed of  $20 \times 20 \times 20$  cubic Cesium Iodide (CsI) crystals with 3.6 cm side for a total depth of  $39 X_0$  have been performed, showing e/p separation factors close to  $10^5$  achieved with the standalone information from the calorimeter. Since the ALADInO calorimeter will be much deeper, will have a similar segmentation, and will profit also from the independent measurement of the particle rigidity with the spectrometer in the TeV energy range, we expect to reach a e/p separation capability of at least  $10^5$ .

#### 4.3. Time-of-Flight (ToF)

The ALADInO ToF system is designed to (a) measure the particle velocity magnitude, with an accuracy of  $\mathcal{O}(\%)$ , and direction; (b) independently measure the particle charge at the entrance and exit surfaces of the tracking volume; and (c) provide the charged-particle fast-signal used to trigger the data acquisition.

The design of the ToF system is based on previous PAMELA [169] and AMS [170] plastic scintillator ToF systems that had similar purposes. Plastic scintillator counters are detection devices ubiquitous in high-energy particle physics that allow for fast signal, high light-yields, long durability, and low cost.

The ALADInO ToF system baseline design is composed by two rings above and below the tracking volume (i.e., the *outer* and *inner* ToF). Each ToF ring is constituted by 10 identical planar detection units, i.e., ToF planes, each one equipped with a double layer of 0.8 cm thick plastic scintillators. Details of the ToF layout can be seen in Figure 15. The single outer ToF detection unit is composed by a support structure of  $190 \times 130 \text{ cm}^2$ . On top of it, 13 plastic scintillator bars of  $190 \times 10 \text{ cm}^2$  are arranged along the detector z-axis; on the other side of the support, 19 scintillator bars of  $130 \times 10 \text{ cm}^2$  are arranged in orthogonal direction. Similarly, the single inner ToF detection unit is composed by a planar support structure of  $90 \times 30 \text{ cm}^2$ , which hosts 3 scintillator bars of  $90 \times 10 \text{ cm}^2$  aligned with the detector z-axis on one side, and 9 scintillator bars of  $10 \times 30 \text{ cm}^2$  arranged in the orthogonal direction on the other side. This geometry provides each ToF plane with coarse  $x - y$  measurement capability. The ToF features in total 440 bars, for a global active area of about  $54.8 \text{ m}^2$ . A possible alternative solution to reduce the scintillator counters length below 1 m is to halve along the length the bars hosted in the outer ToF ring. The total number of scintillator bars in this configuration increases to 760. With the chosen scintillator thickness, the weight of the active material for the ToF amounts to  $\sim 450 \text{ kg}$ . Feasibility studies may confirm the opportunity to equip the ToF with thinner detectors while keeping high performances in charge and velocity measurements, and reducing the contribution of the ToF to the instrument mass. Scintillators with 0.5 cm-thickness would result in a loss in weight of approximately  $\sim 200 \text{ kg}$ .

Even if scintillators can be efficiently readout by Photomultiplier Tubes (PMT) that have been reliably used in space, as demonstrated by the PAMELA [169] and AMS [170] ToF systems, the use of Silicon Photomultipliers (SiPM) represents an interesting viable alternative. SiPM are more compact and robust; can be biased with low voltage ( $V < 100 \text{ V}$ ), avoiding the needs of HV power supplies on-board the payload; operate in a wide temperature range; are insensitive to intense magnetic fields; show higher detection efficiencies and similar timing performances to PMTs; and are more cost-effective (see e.g., [171–173] for an extensive review of the SiPM technology). Moreover, the use of SiPM has been subject of intensive R&D in the last years and is foreseen in future cosmic ray measurement missions on balloons [174,175] and on space-borne instruments [176,177].

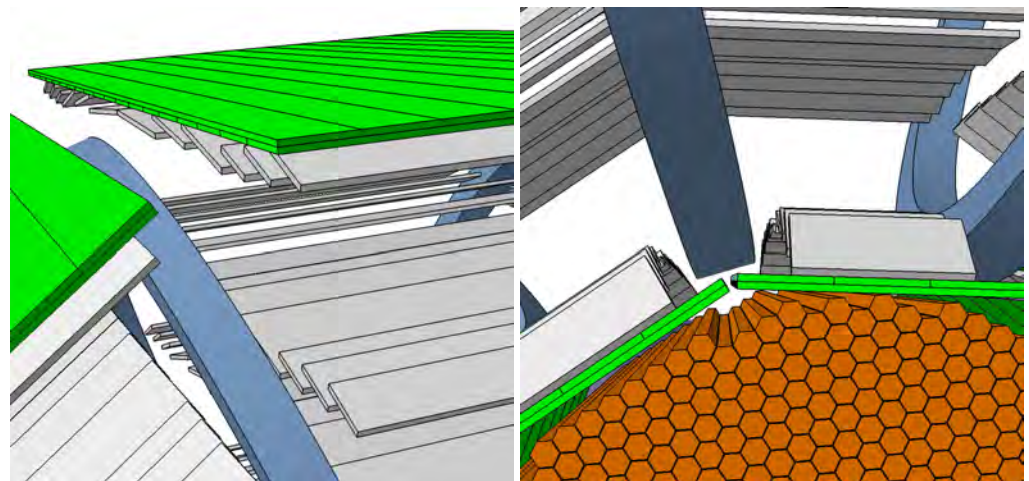


**Figure 15.** Details of the baseline layout proposed for the ToF outer (left) and inner (right) rings. The ToF plastic scintillating counters are shown in green, together with the magnet coils (blue), the silicon tracker sensors (gray), and the calorimeter crystals (orange).

Arrays made of SiPM connected in series and coupled on both sides with scintillators of dimensions similar to those foreseen in the baseline design ( $\sim 1$  m) have shown a counter timing resolution better than 100 ps [178,179]. SiPM coupled to scintillators with smaller dimensions, of few tens of cm, have shown performances reaching 50 ps [180,181] down to  $\sim 40$  ps in ToF instrument demonstrators for space applications in similar conditions to those expected for ALADInO [182]. To push for better timing resolution, the ALADInO ToF bars could be replaced by  $15 \times 15$  cm<sup>2</sup> tiles readout at two opposite corners in both the outer and inner ToF, for an estimated global number of 2580 squared counters.

The ToF timing resolution is of primary importance for the ALADInO physics program. Timing resolutions down to 100 ps or better allow to search for  $\bar{D}$  up to energies where the secondary  $\bar{D}$  spectrum is expected to be more abundant (which is around  $3 \div 4$  GeV/n, see Figure 6). An accurate design of the ToF, as well as a planned R&D activity to investigate the properties of different scintillator modules geometries and different SiPM technologies, may allow reaching a single counter timing resolution better than 100 ps.

A precise charge identification is another important target of the ToF system. Differently from PMT, the response of SiPM is not linear with the increase in light produced by particles with large  $Z$  due to the saturation from concurrent photons converting inside the same pixel: this can be mitigated by choosing SiPM with small pixel size in order to increase the number of cells for a given surface, or by increasing the number of SiPM coupled to the scintillator [180,181]. Prototypes of high-density SiPM with microcell-size below 12.5  $\mu$ m and photo-detection efficiency between 20% and 40% over the visible light range are already available [183], which, coupled to a high-range FEE, could potentially allow for high-range charge measurements up to Iron ( $Z = 26$ ) and above. Decreasing the microcell size will also improve the endurance against radiation damage [184], which is a limiting factor in space [185]. The assessment of radiation damage of SiPM when exposed to an environment representative of that in space is being investigated by exposure of the sensors to proton and heavy ion beams [174,186,187].

Studies of charge resolution with scintillators coupled to SiPM already exist [177,188], showing that separation between elements up to at least  $Z = 10$  is already achievable. A ToF prototype measurement campaign on ion test beam, as the one available at the CERN SPS beam line (see [189]), would be essential to understand the achievable performances.



Temperature plays an important role in the operation of all solid-state devices, including SiPM. Since it affects the gain, noise (dark-current), and also the recovery time of the SiPM [190], temperature is a key parameter to monitor during the operations. During the R&D phase, a detailed study should verify if the planned operation conditions need a temperature feedback on the power supply to monitor and compensate temperature fluctuations (see, e.g., [191,192] and references therein for possible approaches).

The FEE should preserve the intrinsic detector performances in terms of energy and time of arrival measurements together with trigger capabilities. One viable and available readout ASIC for time-of-flight applications are the PETIROC 2A and TRIROC 1A chip series provided by WEEROOC [193]. The PETIROC 2A [194] chip is designed to readout up to 32 SiPM combining a very fast and low-jitter trigger with accurate charge and time measurements (below 40 ps) with a power consumption of 6 mW/channel. Considering such consumption as a reference benchmark for fast-timing readout, the high segmented layout for the ToF bars, and a double readout system for the high dynamic range required for charge measurement of nuclei, this results in a total power consumption for the ToF of approximately 400 W, including DAQ. This, although not dominating the total power budget of the instrument (see Section 4.4), has a robust perspective to be further mitigated with additional advancements in SiPM readout approaches.

In the near future, ToF performances could further improve by taking advantage of ASIC developments from new applications for high-energy physics, medical imaging, and space applications (see, e.g., [195]). An example is the LIROC ASIC currently under development by WEEROOC, for measurement of Lidar in space [196]. It is designed to readout 64 channels with triggering capabilities down to 1/3 p.e. and low-voltage differential trigger output for each channel with an excellent timing resolution (better than 20 ps FWHM) and power consumption of about 3 mW/channel.

#### 4.4. Power Budget

The innovative design of the ALADInO instrument and of its subsystem layouts has been optimized also to constrain the power consumption by the most demanding detectors and services. The most consuming detector subsystem is the tracker, which with  $\sim 2$  M silicon microstrip channels results in a total power consumption for the readout FEE and DAQ of about 1.4 kW. The calorimeter is readout through approximately 31 k electronics channels for the readout of each crystal with two photosensors, for an estimated power consumption of about 200 W. The ToF features a maximum power consumption of 400 W, with prospects to be largely mitigated with further R&D for SiPM high speed and large dynamic range readout. Finally, the cryogenic system will consume approximately 1 kW to cool the magnet coils and keep them at the nominal operating temperature.

The total power budget of the baseline ALADInO design amounts to approximately 3 kW. Table 3 provides a summary of the power consumption discussed above. This value is within the expected power availability for the payload. It is mostly based on considerations on the currently available technologies verified for operations in space and it has the potential to be further mitigated by R&D activities ongoing on most of the systems. Improved solutions for the tracking system that open additional scientific opportunities for the ALADInO detector, as discussed in Section 4.1.2, require more power. Their implementation strongly depends on the power availability for the payload and the possible improvements on power mitigation techniques by dedicated R&D activities.



**Table 3.** Summary of expected power budgets for the main services and detectors of the baseline ALADInO instrument. The estimations for the detectors include FEE and DAQ power consumption.

ALADInO Power Budget	
Time of Flight	0.4 kW
Calorimeter	0.2 kW
Si-Tracker	1.4 kW
Cryogenics	1.0 kW
<b>Total</b>	<b>3.0 kW</b>

#### 4.5. Mass Budget

The design of the instrument has been optimized also in terms of weight and dimensions to fit in the limits set for transport and operation in Earth–Sun Lagrange Point L2 using the Ariane heavy-lift launcher (see Section 3). The heaviest part of the ALADInO instrument is the LYSO calorimeter, which weights  $\sim 2.3$  t, including  $\sim 300$  kg for mechanics. The ToF and tracker share the mechanical support structure, and their combined weight amounts to  $\sim 1.5$  t. The mass of the superconducting magnet amounts to  $\sim 1.2$  t for the cold mass and  $\sim 0.3$  t for its auxiliary systems. In addition to this, up to 0.5 t are conservatively allocated to any other element (shield, radiators, etc.) for maintaining the magnet in the required operational conditions. Finally,  $\sim 0.5$  t are allocated for the power, readout, and control electronics of all the subsystems. A summary of the mass budget for the ALADInO instrument is reported in Table 4. The current total mass estimate is thus lower than 6.5 t for the whole payload, which is in the range allowed for the launch opportunity identified, and with prospects for further optimization in the R&D for next years. Although a more advanced design of the instrument will be produced to provide a more reliable estimate, this result provides a first robust confirmation on the feasibility to host an instrument such as ALADInO in a space vector for its deployment in L2.

**Table 4.** Summary of expected mass budgets for the main services and detectors of the baseline ALADInO instrument. The total payload mass results below the limit for transport in L2 with the Ariane heavy-lift rocket. See text (Section 4.5) for additional details on the mass allocations.

ALADInO Mass Budget	
Calorimeter	$\sim 2.3$ t
Magnet and Cryogenics	$\sim 2.0$ t
Time of Flight + Si-Tracker	$\sim 1.5$ t
Electronics and Power	$\sim 0.5$ t
<b>Total</b>	<b>&lt;6.5 t</b>

### 5. Prospects to Enable the ALADInO Mission

Considering the complexity of the proposed detector layout, as well of the R&D activities foreseen to enable operations of low TRL technologies and novel approaches in space, a possible technological pathfinder mission in L2 is envisaged to pave the way for a large scale mission [96]. The main goal of the ALADInO pathfinder will be to verify the operations in orbit of the spectrometer based on a superconducting magnet, a technology that has never been successfully operated in space, in a simplified layout with contained weight, dimensions, and power consumption. Although mainly thought as a technological demonstrator, the ALADInO pathfinder in L2 will be able to also anticipate the complete physics program of ALADInO in those channels that do not require the measurement of the calorimeter, as similarly done by the prototype AMS-01 flight on the Space Shuttle for the space-verification of the technologies of the operating AMS-02 instrument. The details of the planning for the ALADInO pathfinder will be the objective of a future publication.

After demonstrating the technology readiness with the pathfinder, the operation of ALADInO in the Sun–Earth L2 Lagrangian point for at least 5 years would enable unique

observations with groundbreaking discovery potentials in the field of astroparticle physics providing precise measurements of electrons, positrons, and antiprotons up to 10 TeV and of nuclear cosmic rays up to the PeV scale, and by the possible unambiguous detection and measurement of low-energy antideuteron and antihelium components in cosmic rays.

Such findings will provide unprecedented insights in the frontier of cosmic ray physics, with the potential for groundbreaking discoveries out of reach for AMS-02, the only spectrometer in operation in space today. No spectrometric missions are planned after AMS-02, meaning that there will be no opportunity to shed light on the unexplored frontiers of high energy and very rare cosmic rays. The ALADInO project, although requiring ambitious developments to enable novel technological solutions in space, represents a credible possibility to operate in a finite timescale a lightweight, yet most accurate spectrometric detector. R&D activities to develop, test, and optimize for space operations the required technologies are already progressing in an international effort that takes advantage of the heritage of established space activities and also builds on the advances in complementary, yet synergic, activities in progress at forefront institutions such as CERN, INFN, etc. A well-established network of expertise, activities, and collaborations from academic, research, and industrial realities exists and can be exploited to enable the possibility to construct and deploy in space a groundbreaking experiment such as ALADInO.

The ALADInO concept meets the constraints of space vectors that are available today for transport to L2, independently on the advances to improve the performances and carrying capabilities of space vectors. Considering the current propitious conditions that are already available nowadays in terms of instrumentation technology, space operation heritages, and space vectors, it is possible to envisage that the ALADInO pathfinder could be operating in the 2030s, opening the way for ALADInO operations in the 2040s. In a few years of operations, by 2050, ALADInO will have provided unique data to improve our understanding and possibly solve two of the most subtle yet prominent puzzles of the century: the missing antimatter in the Universe and the nature of Dark Matter.

**Author Contributions:** Conceptualization, G.A. (Giovanni Ambrosi), R.B. (Roberto Battiston), B.B. (Bruna Bertucci), A.C. (Andrea Contin), M.D. (Matteo Duranti), R.I. (Roberto Iuppa), M.N.M. (Mario Nicola Mazziotta), R.M. (Riccardo Musenich), A.O. (Alberto Oliva), P.P. (Paolo Papini), M.P. (Michele Pozzato), and V.V. (Valerio Vagelli); software, N.M. (Nicola Mori); software (instrument simulation), V.C. (Valerio Calvelli), M.D. (Matteo Duranti), V.F. (Valerio Formato), and P.P. (Paolo Papini); formal analysis (measurement perspectives), V.D.F. (Valeria Di Felice), F.N. (Francesco Nozzoli), N.M. (Nicolò Masi), N.T. (Nicola Tomassetti), and V.V. (Valerio Vagelli); writing—original draft preparation, M.D. (Matteo Duranti), R.I. (Roberto Iuppa), M.N.M. (Mario Nicola Mazziotta), R.M. (Riccardo Musenich), A.O. (Alberto Oliva), P.P. (Paolo Papini), and V.V. (Valerio Vagelli); writing—review and editing, O.A. (Oscar Adriani), B.B. (Bertrand Baudouy), F.C.T.B. (Felicia Carla Tiziana Barbato), M.B. (Mirko Boezio), J.C. (Jorge Casaus), V.C. (Valerio Calvelli), A.D.G. (Adriano Di Giovanni), M.D. (Matteo Duranti), F.M.F. (Francesco Maria Follega), R.I. (Roberto Iuppa), N.M. (Nicolò Masi), M.N.M. (Mario Nicola Mazziotta), N.M. (Nicola Mori), R.M. (Riccardo Musenich), L.M. (Lorenzo Mussolin), A.O. (Alberto Oliva), L.P. (Lorenzo Pacini), P.P. (Paolo Papini), C.P. (Cecilia Pizzolotto), and V.V. (Valerio Vagelli); visualization, F.C. (Franck Cadoux) and M.G. (Maura Graziani); investigation, all authors; project administration, R.B. (Roberto Battiston) and B.B. (Bruna Bertucci). All authors have read and agreed to the published version of the manuscript.

**Funding:** This research received no external funding.

**Institutional Review Board Statement:** Not applicable.

**Informed Consent Statement:** Not applicable.

**Data Availability Statement:** Not applicable.

**Conflicts of Interest:** The authors declare no conflict of interest.

## Abbreviations

The following abbreviations are used in this manuscript:

ASIC	Application-Specific Integrated Circuit
CFRP	Carbon Fiber Reinforced Polymer
CsI	Cesium Iodide
CMOS	Complementary metal-oxide-semiconductor
CR	Cosmic Rays
DAQ	Data Acquisition
DM	Dark Matter
FEE	Front-End Electronics
FWHM	Full Width at Half Maximum
FPGA	Field Programmable Gate Array
GPU	Graphics Processing Unit
HTS	High Temperature Superconductors
ISS	International Space Station
L2	Earth–Sun Lagrange Point 2
LGAD	Low-Gain Avalanche Diode
LYSO	Lutetium Yttrium Orthosilicate
MAPS	Monolithic Active Pixel Sensors
MDR	Maximum Detectable Rigidity
MIP	Minimum Ionizing Particles
MLI	Multilayer Insulation
MQE	Minimum Quenching Energy
MRI	Magnetic Resonance Imaging
PMT	Photomultiplier Tube
ReBCO	Rare-earth Barium Copper Oxide
R&D	Research and Development
SiPM	Silicon Photomultiplier
SR2S	Space Radiation Superconducting Shield
ToF	Time-of-flight
TRL	Technology Readiness Level
UFSD	Ultra-Fast Silicon Diode

## Appendix A. AMS-02 Sensitivity to Antideuteron

In Section 2, the AMS-02 sensitivity to  $\bar{D}$  measurements is reported to be approximately  $4 \cdot 10^{-7} (\text{GeV}/n)^{-1} \text{m}^{-2} \text{s}^{-1} \text{sr}^{-1}$  [110]. The reader should note that the aforementioned  $\bar{D}$  sensitivity of AMS-02 is based on a preliminary estimation by the AMS collaboration based on a detector layout with a superconducting magnet, different from that currently in operation in space. A recalculation of this sensitivity estimation based on updated mission measurement time, geomagnetic cutoff model, and background fluxes is available in [197].

## Appendix B. Transition Radiation Detector

Transition Radiation Detectors (TRDs) are currently used in many accelerator and cosmic-ray experiments to discriminate between different charged particles with the same momentum (i.e., electrons against hadrons). Transition Radiation (TR) is emitted in the X-ray region by ultra-relativistic particles crossing the interface between two regions with different dielectric constants [198]. A standard TRD consists of a radiator and an X-ray detector—usually a gaseous counter. The TR yield is roughly proportional to the Lorentz factor  $\gamma$  of the radiating particle over a wide range of  $\gamma$ , typically spanning over one order of magnitude [199]. In particular, TRDs are mostly used to provide e/p separation in a momentum range up to about 1 TV/c [18].

A silicon TRD (SiTRD), employing silicon strip detectors (SSDs) to detect TR X-rays, could be added to the ALADiNO instrument to expand its measurement capabilities. This will work if the detector is located inside a magnetic field region. In fact, the magnetic field separates the radiating particles from the TR X-rays, which are absorbed in a detector

region far apart from the region where the particle deposits its ionization energy. In the past years, several beam tests were carried out on reduced-scale prototypes to study the particle identification performances of the SiTRD technology [200–202].

A multiple-module SiTRD for ALADInO could be implemented inserting radiator layers in front of each tracker plane. This layout would imply the introduction of small amounts of materials (less than 1% radiation length) in the tracker that, however, are expected to not affect significantly its tracking performance. The momentum interval where the SiTRD can identify radiating particles (electrons) from nonradiating ones (protons) is determined by the choice of the radiator and its geometry, by the distance between the tracking planes, and by the granularity of the tracker. Operating the SiTRD on ALADInO allows to provide additional information to discriminate  $e^\pm$  from protons in an energy range up to 1 TeV to that provided by the calorimeter. Since the presence of the magnetic field makes the two measurements independent, the SiTRD information may allow to disentangle the irreducible proton contamination in the calorimeter due to early interacting protons producing high energetic  $\pi_0$ . The combined calorimeter plus TRD e/p separation has been already successfully applied in space instruments (see e.g., [203] for an early approach in a balloon-borne magnetic spectrometer). Very recently, the results from the AMS collaboration have indicated that the combined information from calorimeter and TRD can be used to achieve negligible systematic uncertainties due to residual proton background contamination in the  $e^\pm$  measurement [54,55]. The state-of-the-art TRD operated in space is that of the AMS-02 instrument. It is a gas-based detector made of a stack of proportional tubes interleaved by radiators for TR X-rays detection [54], which provides e/p separation better than  $10^3$  up to energies of 400 GeV and  $10^2$  at 1 TeV [4]. While these performances may be used as a benchmark, possible optimization of the radiator and of the TR X-rays detector of the SiTRD may allow the extension of the highest energy at which  $e^\pm$  can be efficiently separated from protons. Moreover, the use of a solid-state device strongly improves the safety and long-term stability of the detector performances.

## References

1. Atwood, W.B.; Abdo, A.A.; Ackermann, M.; Althouse, W.; Anderson, B.; Axelsson, M.; Baldini, L.; Ballet, J.; Band, D.L.; Barbiellini, G.; et al. The Large Area Telescope on the Fermi Gamma-Ray Space Telescope Mission. *Astrophys. J.* **2009**, *697*, 1071–1102. [[CrossRef](#)]
2. Adriani, O.; Barbarino, G.; Bazilevskaya, G.; Bellotti, R.; Boezio, M.; Bogomolov, E.; Bonghi, M.; Bonvicini, V.; Bottai, S.; Bruno, A.; et al. The PAMELA Mission: Heralding a new era in precision cosmic ray physics. *Phys. Rep.* **2014**, *544*, 323–370. [[CrossRef](#)]
3. Aguilar, M.; Alcaraz, J.; Allaby, J.; Alpat, B.; Ambrosi, G.; Anderhub, H.; Ao, L.; Arefiev, A.; Azzarello, P.; Babucci, E.; et al. The Alpha Magnetic Spectrometer (AMS) on the International Space Station: Part I—results from the test flight on the space shuttle. *Phys. Rep.* **2002**, *366*, 331–405. [[CrossRef](#)]
4. Aguilar, M.; Ali Cavazonza, L.; Ambrosi, G.; Arruda, L.; Attig, N.; Barao, F.; Barrin, L.; Bartoloni, A.; Başegmez-du Pree, S.; Bates, J.; et al. The Alpha Magnetic Spectrometer (AMS) on the international space station: Part II—Results from the first seven years. *Phys. Rep.* **2021**, *894*, 1–116. [[CrossRef](#)]
5. Chang, J.; Ambrosi, G.; An, Q.; Asfandiyarov, R.; Azzarello, P.; Bernardini, P.; Bertucci, B.; Cai, M.; Caragiulo, M.; Chen, D.; et al. The DArk Matter Particle Explorer mission. *Astropart. Phys.* **2017**, *95*, 6–24. [[CrossRef](#)]
6. Marrocchesi, P.S. CALET on the ISS: A high energy astroparticle physics experiment. *J. Phys. Conf. Ser.* **2016**, *718*, 052023. [[CrossRef](#)]
7. Turundaevskiy, A.N.; Vasiliev, O.A.; Karmanov, D.E.; Kovalev, I.M.; Kudryashov, I.A.; Kurganov, A.A.; Panov, A.D.; Podorozhny, D.M. Main Results from the NUCLEON Experiment. *Bull. Russ. Acad. Sci. Phys.* **2021**, *85*, 353–356. [[CrossRef](#)]
8. Seo, E.S.; Aggarwal, S.; Amare, Y.; Angelaszek, D.; Bowman, D.P.; Chen, Y.; Choi, G.H.; Copley, M.; Derome, L.; Eraud, L.; et al. Results from the Cosmic Ray Energetics And Mass for the International Space Station (ISS-CREAM) experiment. In Proceedings of the 37th International Cosmic Ray Conference—PoS(ICRC2021), Berlin, Germany, 12–23 July 2021; Volume 395, p. 95. [[CrossRef](#)]
9. Gabici, S.; Evoli, C.; Gaggero, D.; Lipari, P.; Mertsch, P.; Orlando, E.; Strong, A.; Vittino, A. The origin of Galactic cosmic rays: Challenges to the standard paradigm. *Int. J. Mod. Phys. D* **2019**, *28*, 1930022. [[CrossRef](#)]
10. Herms, J.; Ibarra, A.; Vittino, A.; Wild, S. Antideuterons in cosmic rays: Sources and discovery potential. *J. Cosmol. Astropart. Phys.* **2017**, *2017*, 018. [[CrossRef](#)]

11. Yamamoto, A.; Anraku, K.; Golden, R.; Haga, T.; Higashi, Y.; Imori, M.; Inaba, S.; Kimbell, B.; Kimura, N.; Makida, Y.; et al. Balloon-borne experiment with a superconducting solenoidal magnet spectrometer. *Adv. Space Res.* **1994**, *14*, 75–87. [\[CrossRef\]](#)
12. Lübelmeyer, K.; Schultz von Dratzig, A.; Wlochal, M.; Ambrosi, G.; Azzarello, P.; Battiston, R.; Becker, R.; Becker, U.; Bertucci, B.; Bollweg, K.; et al. Upgrade of the Alpha Magnetic Spectrometer (AMS-02) for long term operation on the International Space Station (ISS). *Nucl. Instrum. Methods Phys. Res. Sect. A Accel. Spectrometers Detect. Assoc. Equip.* **2011**, *654*, 639–648. [\[CrossRef\]](#)
13. Musenich, R.; Becker, R.; Bollweg, K.; Burger, J.; Capell, M.; Datskov, V.I.; Gallilee, M.A.; Gargiulo, C.; Kounine, A.; Koutsenko, V.; et al. Results From the Testing of the AMS Space Superconducting Magnet. *IEEE Trans. Appl. Supercond.* **2012**, *22*, 4500204 [\[CrossRef\]](#)
14. Giovacchini, F. Space application: The AMS RICH. *Nucl. Instrum. Methods Phys. Res. Sect. A Accel. Spectrometers Detect. Assoc. Equip.* **2020**, *970*, 163657. [\[CrossRef\]](#)
15. Stozhkov, Y.I. The in-flight performance of the PAMELA Neutron Detector. In Proceedings of the 30th International Cosmic Ray Conference—PoS(ICRC2007), Mérida, Yucatán, Mexico, 3–11 July 2007; Volume 2, pp. 325–328.
16. Huang, Y.Y.; Ma, T.; Yue, C.; Zhang, Y.; Cai, M.S.; Chang, J.; Dong, T.K.; Zhang, Y.Q. Calibration and performance of the neutron detector onboard of the DAMPE mission. *Res. Astron. Astrophys.* **2020**, *20*, 153. [\[CrossRef\]](#)
17. Doetinchem, P.v.; Fopp, S.; Karpinski, W.; Kim, T.; Lübelmeyer, K.; Orboeck, J.; Schael, S.; Schultz von Dratzig, A.; Schwering, G.; Siedenburt, T.; et al. Performance of the AMS-02 transition radiation detector. *Nucl. Instrum. Methods Phys. Res. Sect. A Accel. Spectrometers Detect. Assoc. Equip.* **2006**, *558*, 526–535. [\[CrossRef\]](#)
18. Kim, T. The AMS-02 TRD on the international space station. *Nucl. Instrum. Methods Phys. Res. Sect. A Accel. Spectrometers Detect. Assoc. Equip.* **2013**, *706*, 43–47. [\[CrossRef\]](#)
19. Ambriola, M. Performance of the transition radiation detector of the PAMELA space mission. *Nucl. Phys. B-Proc. Suppl.* **2002**, *113*, 322–328. [\[CrossRef\]](#)
20. Ackermann, M.; Ajello, M.; Allafort, A.; Atwood, W.B.; Baldini, L.; Barbiellini, G.; Bastieri, D.; Bechtol, K.; Bellazzini, R.; Berenji, B.; et al. Measurement of Separate Cosmic-Ray Electron and Positron Spectra with the Fermi Large Area Telescope. *Phys. Rev. Lett.* **2012**, *108*, 011103. [\[CrossRef\]](#)
21. Ong, R.; Aramaki, T.; Bird, R.; Boezio, M.; Boggs, S.E.; Carr, R.; Craig, W.; Von Doetinchem, P.; Fabris, L.; Gahbauer, F.; et al. The GAPS experiment to search for dark matter using low-energy antimatter. In Proceedings of the 35th International Cosmic Ray Conference—PoS(ICRC2017), Bexco, Korea, 12–20 July 2017; Volume 301, p. 914. [\[CrossRef\]](#)
22. Aramaki, T.; Adrian, P.O.H.; Karagiorgi, G.; Odaka, H. Dual MeV gamma-ray and dark matter observatory—GRAMS Project. *Astropart. Phys.* **2020**, *114*, 107–114. [\[CrossRef\]](#)
23. Nozzoli, F.; Dimiccoli, F.; Zuccon, P. Perspectives of dark matter indirect search with ADHD in space. *J. Physics Conf. Ser.* **2020**, *1548*, 012035. [\[CrossRef\]](#)
24. De Shong, J.A.; Hildebrand, R.H.; Meyer, P. Ratio of Electrons to Positrons in the Primary Cosmic Radiation. *Phys. Rev. Lett.* **1964**, *12*, 3–6. [\[CrossRef\]](#)
25. Golden, R.L.; Horan, S.; Mauger, B.G.; Badhwar, G.D.; Lacy, J.L.; Stephens, S.A.; Daniel, R.R.; Zipse, J.E. Evidence for the Existence of Cosmic-Ray Antiprotons. *Phys. Rev. Lett.* **1979**, *43*, 1196–1199. [\[CrossRef\]](#)
26. Earl, J.A. Cloud-Chamber Observations of Primary Cosmic-Ray Electrons. *Phys. Rev. Lett.* **1961**, *6*, 125–128. [\[CrossRef\]](#)
27. Boezio, M.; Munini, R.; Picozza, P. Cosmic ray detection in space. *Prog. Part. Nucl. Phys.* **2020**, *112*, 103765. [\[CrossRef\]](#)
28. Alcaraz, J. A silicon microstrip tracker in space Experience with the AMS silicon tracker on STS-91. *Nuovo Cimento A* **1999**, *112A*, 1325–1343. [\[CrossRef\]](#)
29. Straulino, S.; Adriani, O.; Bonechi, L.; Bonghi, M.; Castellini, G.; D'Alessandro, R.; Gabbanini, A.; Grandi, M.; Papini, P.; Ricciarini, S.; et al. The PAMELA silicon tracker. *Nucl. Instrum. Methods Phys. Res. Sect. A Accel. Spectrometers Detect. Assoc. Equip.* **2004**, *530*, 168–172.
30. Alpat, B.; Ambrosi, G.; Azzarello, P.; Battiston, R.; Bertucci, B.; Bourquin, M.; Burger, W.; Cadoux, F.; da Silva Costa, C.; Choutko, V.; et al. The internal alignment and position resolution of the AMS-02 silicon tracker determined with cosmic-ray muons. *Nucl. Instrum. Methods Phys. Res. Sect. A Accel. Spectrometers Detect. Assoc. Equip.* **2010**, *613*, 207–217. [\[CrossRef\]](#)
31. Zhang, S.N.; Adriani, O.; Consortium, H.; Albergo, S.; Ambrosi, G.; An, Q.; Azzarello, P.; Bai, Y.; Bao, T.; Bernardini, P.; et al. Introduction to the High Energy cosmic-Radiation Detection (HERD) Facility onboard China's Future Space Station. In Proceedings of the 35th International Cosmic Ray Conference—PoS(ICRC2017), Bexco, Korea, 12–20 July 2017; Volume 301, p. 1077. [\[CrossRef\]](#)
32. Schael, S.; Atanasyan, A.; Berdugo, J.; Bretz, T.; Czupalla, M.; Dachwald, B.; von Doetinchem, P.; Duranti, M.; Gast, H.; Karpinski, W.; et al. AMS-100: The next generation magnetic spectrometer in space—An international science platform for physics and astrophysics at Lagrange point 2. *Nucl. Instrum. Methods Phys. Res. Sect. A Accel. Spectrometers Detect. Assoc. Equip.* **2019**, *944*, 162561. [\[CrossRef\]](#)
33. Torii, S. The CALorimetric Electron Telescope (CALET): A High-Energy Astroparticle Physics Observatory on the International Space Stati. In Proceedings of the 34th International Cosmic Ray Conference—PoS(ICRC2015), The Hague, The Netherlands, 30 July–6 August 2015; Volume 236, p. 581. [\[CrossRef\]](#)



34. Ambrosi, G.; An, Q.; Asfandiyarov, R.; Azzarello, P.; Bernardini, P.; Bertucci, B.; Cai, M.S.; Chang, J.; Chen, D.Y.; Chen, H.F.; et al. Direct detection of a break in the teraelectronvolt cosmic-ray spectrum of electrons and positrons. *Nature* **2017**, *552*, 63–66. [CrossRef]
35. National Institute for Nuclear Physics, Press Release. DAMPE: In Search of Dark Matter in Cosmic Rays. 2017. Available online: <https://home.infn.it/en/press-releases/press-release-2017/2705-studiare-i-raggi-cosmici-per-capire-la-materia-oscura-dampe-pubblica-i-primi-risultati-2> (accessed on 1 April 2022).
36. Kounine, A. The Alpha Magnetic Spectrometer on the International Space Station. *Int. J. Mod. Phys. E* **2012**, *21*, 1230005. [CrossRef]
37. Aguilar, M.; Aisa, D.; Alvino, A.; Ambrosi, G.; Andeen, K.; Arruda, L.; Attig, N.; Azzarello, P.; Bachlechner, A.; Barao, F.; et al. Electron and Positron Fluxes in Primary Cosmic Rays Measured with the Alpha Magnetic Spectrometer on the International Space Station. *Phys. Rev. Lett.* **2014**, *113*, 121102. [CrossRef] [PubMed]
38. Aguilar, M.; Aisa, D.; Alpat, B.; Alvino, A.; Ambrosi, G.; Andeen, K.; Arruda, L.; Attig, N.; Azzarello, P.; Bachlechner, A.; et al. Precision Measurement of the ( $e^+ + e^-$ ) Flux in Primary Cosmic Rays from 0.5 GeV to 1 TeV with the Alpha Magnetic Spectrometer on the International Space Station. *Phys. Rev. Lett.* **2014**, *113*, 221102. [CrossRef] [PubMed]
39. Duranti, M. In-flight operations and status of the AMS-02 silicon tracker. In Proceedings of the 34th International Cosmic Ray Conference—PoS(ICRC2015), The Hague, The Netherlands, 30 July–6 August 2015; Volume 236, p. 690. [CrossRef]
40. Perrina, C.. The future of the high energy cosmic ray detection: HERD. *EPJ Web Conf.* **2019**, *209*, 01040. [CrossRef]
41. Blinnikov, S.I.; Dolgov, A.D.; Postnov, K.A. Antimatter and antistars in the Universe and in the Galaxy. *Phys. Rev. D* **2015**, *92*, 023516. [CrossRef]
42. Poulin, V.; Salati, P.; Cholis, I.; Kamionkowski, M.; Silk, J. Where do the AMS-02 antihelium events come from? *Phys. Rev. D* **2019**, *99*, 023016. [CrossRef]
43. Zyla, P.; Barnett, R.M.; Beringer, J.; Dahl, O.; Dwyer, D.A.; Groom, D.E.; Lin, C.-J.; Lugovsky, K.S.; Pianori, E.; Robinson, D.J. et al. Review of Particle Physics. *PTEP* **2020**, *2020*, 083C01. [CrossRef]
44. Bambi, C.; Dolgov, A. Antimatter in the Milky Way. *Nucl. Phys. B* **2007**, *784*, 132–150. [CrossRef]
45. Adriani, O.; Barbarino, G.C.; Bazilevskaya, G.A.; Bellotti, R.; Bianco, A.; Boezio, M.; Bogomolov, E.A.; Bongi, M.; Bonvicini, V.; Bottai, S.; et al. Cosmic-Ray Positron Energy Spectrum Measured by PAMELA. *Phys. Rev. Lett.* **2013**, *111*, 081102. [CrossRef]
46. Aguilar, M.; Ali Cavazonza, L.; Ambrosi, G.; Arruda, L.; Attig, N.; Azzarello, P.; Bachlechner, A.; Barao, F.; Barrau, A.; Barrin, L.; et al. Towards Understanding the Origin of Cosmic-Ray Positrons. *Phys. Rev. Lett.* **2019**, *122*, 041102. [CrossRef]
47. Aguilar, M.; Ali Cavazonza, L.; Alpat, B.; Ambrosi, G.; Arruda, L.; Attig, N.; Aupetit, S.; Azzarello, P.; Bachlechner, A.; Barao, F.; et al. Antiproton Flux, Antiproton-to-Proton Flux Ratio, and Properties of Elementary Particle Fluxes in Primary Cosmic Rays Measured with the Alpha Magnetic Spectrometer on the International Space Station. *Phys. Rev. Lett.* **2016**, *117*, 091103. [CrossRef]
48. Abe, K.; Fuke, H.; Haino, S.; Hams, T.; Itazaki, A.; Kim, K.; Kumazawa, T.; Lee, M.; Makida, Y.; Matsuda, S.; et al. Measurement of the cosmic-ray low-energy antiproton spectrum with the first BESS-Polar Antarctic flight. *Phys. Lett. B* **2008**, *670*, 103–108. [CrossRef]
49. Alcaraz, J.; Alvisi, D.; Alpat, B.; Ambrosi, G.; Anderhub, H.; Ao, L.; Arefiev, A.; Azzarello, P.; Babucci, E.; Baldini, L.; et al. Search for antihelium in cosmic rays. *Phys. Lett. B* **1999**, *461*, 387–396. [CrossRef]
50. Chardonnet, P.; Orloff, J.; Salati, P. The production of anti-matter in our galaxy. *Phys. Lett. B* **1997**, *409*, 313–320. [CrossRef]
51. Ting, S.C.C. Latest Results from the AMS Experiment on the International Space Station. In Proceedings of the 69th International Astronautical Congress 2018, Bremen, Germany, 1–5 October 2018.
52. Blum, K.; Ng, K.C.Y.; Sato, R.; Takimoto, M. Cosmic rays, antihelium, and an old navy spotlight. *Phys. Rev. D* **2017**, *96*, 103021. [CrossRef]
53. Adriani, O.; Barbarino, G.C.; Bazilevskaya, G.A.; Bellotti, R.; Boezio, M.; Bogomolov, E.A.; Bonechi, L.; Bongi, M.; Bonvicini, V.; Bottai, S.; et al. An anomalous positron abundance in cosmic rays with energies 1.5–100 GeV. *Nature* **2009**, *458*, 607–609. [CrossRef]
54. Aguilar, M.; Alberti, G.; Alpat, B.; Alvino, A.; Ambrosi, G.; Andeen, K.; Anderhub, H.; Arruda, L.; Azzarello, P.; Bachlechner, A.; et al. First Result from the Alpha Magnetic Spectrometer on the International Space Station: Precision Measurement of the Positron Fraction in Primary Cosmic Rays of 0.5–350 GeV. *Phys. Rev. Lett.* **2013**, *110*, 141102. [CrossRef]
55. Accardo, L.; Aguilar, M.; Aisa, D.; Alpat, B.; Alvino, A.; Ambrosi, G.; Andeen, K.; Arruda, L.; Attig, N.; Azzarello, P.; et al. High Statistics Measurement of the Positron Fraction in Primary Cosmic Rays of 0.5–500 GeV with the Alpha Magnetic Spectrometer on the International Space Station. *Phys. Rev. Lett.* **2014**, *113*, 121101. [CrossRef]
56. Cowsik, R.; Burch, B.; Madziwa-Nussinov, T. The origin of the spectral intensities of cosmic-ray positrons. *Astrophys. J.* **2014**, *786*, 124. [CrossRef]
57. Lipari, P. Interpretation of the cosmic ray positron and antiproton fluxes. *Physical Rev. D* **2017**, *95*, 063009. [CrossRef]
58. Blum, K.; Katz, B.; Waxman, E. AMS-02 Results Support the Secondary Origin of Cosmic Ray Positrons. *Phys. Rev. Lett.* **2013**, *111*, 211101. [CrossRef]
59. Turner, M.S.; Wilczek, F. Positron line radiation as a signature of particle dark matter in the halo. *Phys. Rev. D* **1990**, *42*, 1001–1007. [CrossRef] [PubMed]
60. Ellis, J. Particles and cosmology: Learning from cosmic rays. *AIP Conf. Proc.* **2000**, *516*, 21–46. [CrossRef]

61. Cheng, H.C.; Feng, J.L.; Matchev, K.T. Kaluza-Klein Dark Matter. *Physical Rev. Lett.* **2002**, *89*, 211301. [[CrossRef](#)] [[PubMed](#)]
62. Kane, G.; Lu, R.; Watson, S. PAMELA satellite data as a signal of non-thermal wino LSP dark matter. *Phys. Lett. B* **2009**, *681*, 151–160. [[CrossRef](#)]
63. Kopp, J. Constraints on dark matter annihilation from AMS-02 results. *Physical Rev. D* **2013**, *88*, 076013. [[CrossRef](#)]
64. Chen, C.H.; Chiang, C.W.; Nomura, T. Dark matter for excess of AMS-02 positrons and antiprotons. *Phys. Lett. B* **2015**, *747*, 495–499. [[CrossRef](#)]
65. Cheng, H.C.; Huang, W.C.; Huang, X.; Low, I.; Tsai, Y.L.S.; Yuan, Q. AMS-02 positron excess and indirect detection of three-body decaying dark matter. *J. Cosmol. Astropart. Phys.* **2017**, *2017*, 041. [[CrossRef](#)]
66. Bai, Y.; Berger, J.; Lu, S. Supersymmetric resonant dark matter: A thermal model for the AMS-02 positron excess. *Phys. Rev. D* **2018**, *97*, 115012. [[CrossRef](#)]
67. Profumo, S.; Queiroz, F.; Siqueira, C. Has AMS-02 observed two-component dark matter? *J. Phys. G: Nucl. Part. Phys.* **2020**, *48*, 015006. [[CrossRef](#)]
68. Serpico, P.D. Astrophysical models for the origin of the positron “excess”. *Astropart. Phys.* **2012**, *39–40*, 2–11. [[CrossRef](#)]
69. Linden, T.; Profumo, S. Probing the pulsar origin of the anomalous positron fraction with AMS-02 and atmospheric Cherenkov telescopes. *Astrophys. J.* **2013**, *772*, 18. [[CrossRef](#)]
70. Mertsch, P.; Sarkar, S. AMS-02 data confront acceleration of cosmic ray secondaries in nearby sources. *Phys. Rev. D* **2014**, *90*, 061301. [[CrossRef](#)]
71. Tomassetti, N.; Donato, F. The connection between the positron fraction anomaly and the spectral features in galactic cosmic-ray hadrons. *Astrophys. J.* **2015**, *803*, L15. [[CrossRef](#)]
72. Hooper, D.; Cholis, I.; Linden, T.; Fang, K. HAWC observations strongly favor pulsar interpretations of the cosmic-ray positron excess. *Phys. Rev. D* **2017**, *96*, 103013. [[CrossRef](#)]
73. Liu, W.; Bi, X.J.; Lin, S.J.; Wang, B.B.; Yin, P.F. Excesses of cosmic ray spectra from a single nearby source. *Phys. Rev. D* **2017**, *96*, 023006. [[CrossRef](#)]
74. Bykov, A.M.; Amato, E.; Petrov, A.E.; Krassilchtchikov, A.M.; Levenfish, K.P. Pulsar Wind Nebulae with Bow Shocks: Non-thermal Radiation and Cosmic Ray Leptons. *Space Sci. Rev.* **2017**, *207*, 235–290. [[CrossRef](#)]
75. Kachelrieß, M.; Neronov, A.; Semikoz, D.V. Cosmic ray signatures of a 2–3 Myr old local supernova. *Phys. Rev. D* **2018**, *97*, 063011. [[CrossRef](#)]
76. Profumo, S.; Reynoso-Cordova, J.; Kaaz, N.; Silverman, M. Lessons from HAWC pulsar wind nebulae observations: The diffusion constant is not a constant; pulsars remain the likeliest sources of the anomalous positron fraction; cosmic rays are trapped for long periods of time in pockets of inefficient diffusion. *Phys. Rev. D* **2018**, *97*, 123008. [[CrossRef](#)]
77. Manconi, S.; Mauro, M.D.; Donato, F. Dipole anisotropy in cosmic electrons and positrons: Inspection on local sources. *J. Cosmol. Astropart. Phys.* **2017**, *2017*, 006. [[CrossRef](#)]
78. Fang, K.; Bi, X.J.; Yin, P.F. Discriminating local sources of high-energy cosmic electrons and positrons by current and future anisotropy measurements. *Mon. Not. R. Astron. Soc.* **2018**, *478*, 5660–5670. [[CrossRef](#)]
79. Giesen, G.; Boudaud, M.; Génolini, Y.; Poulin, V.; Cirelli, M.; Salati, P.; Serpico, P.D. AMS-02 antiprotons, at last! Secondary astrophysical component and immediate implications for Dark Matter. *J. Cosmol. Astropart. Phys.* **2015**, *2015*, 023. [[CrossRef](#)]
80. Evoli, C.; Gaggero, D.; Grasso, D. Secondary antiprotons as a Galactic Dark Matter probe. *J. Cosmol. Astropart. Phys.* **2015**, *2015*, 039. [[CrossRef](#)]
81. Cui, M.Y.; Yuan, Q.; Tsai, Y.L.S.; Fan, Y.Z. Possible Dark Matter Annihilation Signal in the AMS-02 Antiproton Data. *Phys. Rev. Lett.* **2017**, *118*, 191101. [[CrossRef](#)]
82. Cuoco, A.; Krämer, M.; Korsmeier, M. Novel Dark Matter Constraints from Antiprotons in Light of AMS-02. *Phys. Rev. Lett.* **2017**, *118*, 191102. [[CrossRef](#)] [[PubMed](#)]
83. Reinert, A.; Winkler, M.W. A precision search for WIMPs with charged cosmic rays. *J. Cosmol. Astropart. Phys.* **2018**, *2018*, 055. [[CrossRef](#)]
84. Cholis, I.; Linden, T.; Hooper, D. A robust excess in the cosmic-ray antiproton spectrum: Implications for annihilating dark matter. *Phys. Rev. D* **2019**, *99*, 103026. [[CrossRef](#)]
85. Donato, F.; Korsmeier, M.; Di Mauro, M. Prescriptions on antiproton cross section data for precise theoretical antiproton flux predictions. *Phys. Rev. D* **2017**, *96*, 043007. [[CrossRef](#)]
86. Boschini, M.J.; Torre, S.D.; Gervasi, M.; Grandi, D.; Jóhannesson, G.; Kachelrieß, M.; Vacca, G.L.; Masi, N.; Moskalenko, I.V.; Orlando, E.; et al. Solution of Heliospheric Propagation: Unveiling the Local Interstellar Spectra of Cosmic-ray Species. *Astrophys. J.* **2017**, *840*, 115. [[CrossRef](#)]
87. Bresci, V.; Amato, E.; Blasi, P.; Morlino, G. Effects of re-acceleration and source grammage on secondary cosmic rays spectra. *Mon. Not. R. Astron. Soc.* **2019**, *488*, 2068–2078. [[CrossRef](#)]
88. Donato, F.; Fornengo, N.; Salati, P. Antideuterons as a signature of supersymmetric dark matter. *Phys. Rev. D* **2000**, *62*, 043003. [[CrossRef](#)]
89. Cirelli, M.; Fornengo, N.; Taoso, M.; Vittino, A. Anti-helium from dark matter annihilations. *J. High Energy Phys.* **2014**, *2014*, 9. [[CrossRef](#)]
90. Carlson, E.; Coogan, A.; Linden, T.; Profumo, S.; Ibarra, A.; Wild, S. Antihelium from dark matter. *Phys. Rev. D* **2014**, *89*, 076005. [[CrossRef](#)]

91. Cholis, I.; Linden, T.; Hooper, D. Antideuterons and antihelium nuclei from annihilating dark matter. *Phys. Rev. D* **2020**, *102*. [CrossRef]
92. McElwain, M.W.; Niedner, M.B.; Bowers, C.W.; Kimble, R.A.; Smith, E.C.; Clampin, M. The James Webb Space telescope: Observatory status and preparations for launch (Conference Presentation). In *Space Telescopes and Instrumentation 2018: Optical, Infrared, and Millimeter Wave*; Lystrup, M., MacEwen, H.A., Fazio, G.G., Batalha, N., Siegler, N., Tong, E.C., Eds.; International Society for Optics and Photonics, SPIE: Bellingham, WA, USA, 2018; Volume 10698. [CrossRef]
93. Berdugo, J.; Choutko, V.; Delgado, C.; Yan, Q. Determination of the rigidity scale of the Alpha Magnetic Spectrometer. *Nucl. Instrum. Methods Phys. Res. Sect. A Accel. Spectrometers Detect. Assoc. Equip.* **2017**, *869*, 10–14. [CrossRef]
94. Zang, J.; Yue, C.; Li, X. Measurement of absolute energy scale of ECAL of DAMPE with geomagnetic rigidity cutoff. In *Proceedings of the 35th International Cosmic Ray Conference—PoS(ICRC2017)*, Bexco, Korea, 12–20 July 2017; Volume 301, p. 197. [CrossRef]
95. Adriani, O.; Akaïke, Y.; Asano, K.; Asaoka, Y.; Bagliesi, M.G.; Bigongiari, G.; Binns, W.R.; Bonechi, S.; Bongi, M.; Brogi, P.; et al. Energy Spectrum of Cosmic-Ray Electron and Positron from 10 GeV to 3 TeV Observed with the Calorimetric Electron Telescope on the International Space Station. *Phys. Rev. Lett.* **2017**, *119*, 181101. [CrossRef]
96. Battiston, R.; Bertucci, B.; Adriani, O.; Ambrosi, G.; Baudouy, B.; Blasi, P.; Boezio, M.; Campana, D.; Derome, L.; De Mitri, I.; et al. High precision particle astrophysics as a new window on the universe with an Antimatter Large Acceptance Detector In Orbit (ALADInO). *Exp. Astron.* **2021**, *51*, 1299–1330. [CrossRef]
97. Duranti, M. The AMS-02 Silicon Tracker (The Detector after 500 Days in Space). In *Proceedings of the 21st International Workshop on Vertex Detectors—PoS(Vertex 2012)*, Jeju, Korea, 16–21 September 2012; Volume 167, p. 52. [CrossRef]
98. NASA. Roman Space Telescope Observatory Reference Information. Available online: [https://roman.gsfc.nasa.gov/science/Roman\\_Reference\\_Information.html](https://roman.gsfc.nasa.gov/science/Roman_Reference_Information.html), (accessed on 8 January 2022).
99. Christine Pulliam. 2021. Available online: <https://www.nasa.gov/feature/goddard/2021/ground-system-for-nasa-s-roman-space-telescope-moves-into-development>, (accessed on 8 January 2022).
100. Johns, A.; Seaton, B.; Gal-Edd, J.; Jones, R.; Fatig, C.; Wasiak, F. James Webb Space Telescope: L2 communications for science data processing. In *Observatory Operations: Strategies, Processes, and Systems II*; Society of Photo-Optical Instrumentation Engineers (SPIE) Conference Series; Brissenden, R.J., Silva, D.R., Eds.; SPIE: Bellingham, WA, USA, 2008; Volume 7016, p. 70161D. [CrossRef]
101. Dubath, P.; Apostolakis, N.; Bonchi, A.; Belikov, A.; Brescia, M.; Caviuoti, S.; Capak, P.; Coupon, J.; Dabin, C.; Degaudenzi, H.; et al. The Euclid Data Processing Challenges. *Proc. Int. Astron. Union* **2017**, *12*. [CrossRef]
102. Mori, N. GGS: A Generic Geant4 Simulation package for small- and medium-sized particle detection experiments. *Nucl. Instrum. Methods Phys. Res. Sect. A Accel. Spectrometers Detect. Assoc. Equip.* **2021**, *1002*, 165298. [CrossRef]
103. Sullivan, J. Geometric factor and directional response of single and multi-element particle telescopes. *Nucl. Instrum. Methods* **1971**, *95*, 5–11. [CrossRef]
104. Aguilar, M.; Ali Cavasonza, L.; Alpat, B.; Ambrosi, G.; Arruda, L.; Attig, N.; Azzarello, P.; Bachlechner, A.; Barao, F.; Barrau, A.; et al. Towards Understanding the Origin of Cosmic-Ray Electrons. *Phys. Rev. Lett.* **2019**, *122*, 101101. [CrossRef]
105. Fornieri, O.; Gaggero, D.; Grasso, D. Features in cosmic-ray lepton data unveil the properties of nearby cosmic accelerators. *J. Cosmol. Astropart. Phys.* **2020**, *2020*, 009. [CrossRef]
106. Feng, J.; Zhang, H.H. Pulsar interpretation of lepton spectra measured by AMS-02. *Eur. Phys. J. C* **2016**, *76*, 229. [CrossRef]
107. Büsching, I.; de Jager, O.C.; Potgieter, M.S.; Venter, C. A Cosmic-Ray Positron Anisotropy due to Two Middle-Aged, Nearby Pulsars? *Astrophys. J.* **2008**, *678*, L39–L42. [CrossRef]
108. Jin, H.B.; Wu, Y.L.; Zhou, Y.F. Upper limits on dark matter annihilation cross sections from the first AMS-02 antiproton data. *Phys. Rev. D* **2015**, *92*, 055027. [CrossRef]
109. von Doetinchem, P.; Perez, K.; Aramaki, T.; Baker, S.; Barwick, S.; Bird, R.; Boezio, M.; Boggs, S.; Cui, M.; Datta, A.; et al. Cosmic-ray antinuclei as messengers of new physics: Status and outlook for the new decade. *J. Cosmol. Astropart. Phys.* **2020**, *2020*, 035. [CrossRef]
110. Choutko, V.; Giovacchini, F. Cosmic Rays Antideuteron Sensitivity for AMS-02 Experiment. In *Proceedings of the 30th International Cosmic Ray Conference—PoS(ICRC2007)*, Mérida, Yucatán, Mexico, 3–11 July 2007; Volume 4, pp. 765–768.
111. Aramaki, T.; Hailey, C.J.; Boggs, S.E.; von Doetinchem, P.; Fuke, H.; Mognet, S.I.; Ong, R.A.; Perez, K.; Zweerink, J. Antideuteron sensitivity for the GAPS experiment. *Astropart. Phys.* **2016**, *74*, 6–13. [CrossRef]
112. Coogan, A.; Profumo, S. Origin of the tentative AMS antihelium events. *Physical Rev. D* **2017**, *96*, 083020. PhysRevD.96.083020. [CrossRef]
113. Cowsik, R.; Madziwa-Nussinov, T. Spectral intensities of antiprotons and the nested leaky-box model for cosmic rays in the Galaxy. *Astrophys. J.* **2016**, *827*, 119. [CrossRef]
114. Sakai, K.; Abe, K.; Fuke, H.; Haino, S.; Hams, T.; Hasegawa, M.; Kim, K.; Lee, M.; Makida, Y.; Mitchell, J.; et al. New result of Antideuteron search in BESS-Polar II. In *Proceedings of the 37th International Cosmic Ray Conference—PoS(ICRC2021)*, Berlin, Germany, 12–23 July 2021; Volume 395, p. 123. [CrossRef]
115. Abe, K.; Fuke, H.; Haino, S.; Hams, T.; Hasegawa, M.; Horikoshi, A.; Itazaki, A.; Kim, K.C.; Kumazawa, T.; Kusumoto, A.; et al. Search for Antihelium with the BESS-Polar Spectrometer. *Phys. Rev. Lett.* **2012**, *108*, 131301. [CrossRef]

116. Adriani, O.; Bonechi, L.; Bongi, M.; Castellini, G.; D'Alessandro, R.; Gabbanini, A.; Grandi, M.; Papini, P.B.; Ricciarini, S.; Spillantini, P.; et al. The magnetic spectrometer of the PAMELA satellite experiment. *Nucl. Instrum. Methods Phys. Res. Sect. A Accel. Spectrometers Detect. Assoc. Equip.* **2003**, *511*, 72–75. doi: 10.1016/S0168-9002(03)01754-6. [\[CrossRef\]](#)
117. Viertel, G.; Capell, M. The ALPHA Magnetic Spectrometer. *Nucl. Instrum. Methods Phys. Res. Sect. A Accel. Spectrometers Detect. Assoc. Equip.* **1998**, *419*, 295–299. [\[CrossRef\]](#)
118. Blau, B.; Harrison, S.; Hofer, H.; Horvath, I.; Milward, S.; Ross, J.; Ting, S.; Ulbricht, J.; Viertel, G. The superconducting magnet system of AMS-02—A particle physics detector to be operated on the International Space Station. *IEEE Trans. Appl. Supercond.* **2002**, *12*, 349–352. [\[CrossRef\]](#)
119. Blau, B.; Harrison, S.; Hofer, H.; Milward, S.; Kaiser, G.S.H.; Ross, J.; Ting, S.; Ulbricht, J. The superconducting magnet system of the alpha magnetic spectrometer AMS-02. *Nucl. Instrum. Methods Phys. Res. Sect. A Accel. Spectrometers Detect. Assoc. Equip.* **2004**, *518*, 139–142. [\[CrossRef\]](#)
120. Musenich, R.; Adriani, O.; Baudouy, B.; Calvelli, V.; Farinon, S.; Papini, P.; Bertucci, B. A Proposal for a Superconducting Space Magnet for an Antimatter Spectrometer. *IEEE Trans. Appl. Supercond.* **2020**, *30*, 1–5. [\[CrossRef\]](#)
121. Battiston, R.; Burger, W.J.; Calvelli, V.; Datskov, V.I.; Farinon, S.; Musenich, R. Superconducting Magnets for Astroparticle Shielding in Interplanetary Manned Missions. *IEEE Trans. Appl. Supercond.* **2013**, *23*, 4101604. [\[CrossRef\]](#)
122. Musenich, R.; Calvelli, V.; Farinon, S.; Battiston, R.; Burger, W.J.; Spillantini, P. A Magnesium Diboride Superconducting Toroid for Astroparticle Shielding. *IEEE Trans. Appl. Supercond.* **2014**, *24*, 1–4. [\[CrossRef\]](#)
123. Rossi, L.; Sorbi, M.; Spillantini, P. A superconducting magnetic lens for solar rays protection in manned interplanetary missions. *IEEE Trans. Appl. Supercond.* **2004**, *14*, 1696–1699. [\[CrossRef\]](#)
124. Green, M.; Smoot, G.; Golden, R.; Israel, M.; Kephart, R.; Niemann, R.; Mewalt, R.; Ormes, J.; Spillantini, P.; Wiedenbeck, M. ASTROMAG: A superconducting particle astrophysics magnet facility for the space station. *IEEE Trans. Magn.* **1987**, *23*, 1240–1243. [\[CrossRef\]](#)
125. Dam, M.; Battiston, R.; Burger, W.J.; Carpentiero, R.; Chesta, E.; Iuppa, R.; de Rijk, G.; Rossi, L. Conceptual design of a high temperature superconducting magnet for a particle physics experiment in space. *Supercond. Sci. Technol.* **2020**, *33*, 044012. [\[CrossRef\]](#)
126. OPERA. 2021. Available online: <https://www.3ds.com/products-services/simulia/products/opera/> (accessed on 11 January 2022).
127. Hahn, S.; Park, D.K.; Bascunan, J.; Iwasa, Y. HTS Pancake Coils Without Turn-to-Turn Insulation. *IEEE Trans. Appl. Supercond.* **2011**, *21*, 1592–1595. [\[CrossRef\]](#)
128. SuperPower Inc. 2021. Available online: <https://www.superpower-inc.com/specification.aspx> (accessed on 1 April 2022).
129. Brittles, G.D.; Mousavi, T.; Grovenor, C.R.M.; Aksoy, C.; Speller, S.C. Persistent current joints between technological superconductors. *Supercond. Sci. Technol.* **2015**, *28*, 093001. [\[CrossRef\]](#)
130. Bruce, R.; Baudouy, B. Cryogenic Design of a Large Superconducting Magnet for Astro-particle Shielding on Deep Space Travel Missions. *Phys. Procedia* **2015**, *67*, 264–269. [\[CrossRef\]](#)
131. Ade, P.A.R.; Aghanim, N.; Arnaud, M.; Ashdown, M.; Aumont, J.; Baccigalupi, C.; Baker, M.; Balbi, A.; Banday, A.J.; Barreiro, R.B.; et al. Planck early results. II. The thermal performance of Planck. *Astron. Astrophys.* **2011**, *536*.
132. Arenberg, J.; Flynn, J.; Cohen, A.; Lynch, R.; Cooper, J. Status of the JWST sunshield and spacecraft. In *Space Telescopes and Instrumentation 2016: Optical, Infrared, and Millimeter Wave*; MacEwen, H.A., Fazio, G.G., Lystrup, M., Batalha, N., Siegler, N., Tong, E.C., Eds.; International Society for Optics and Photonics, SPIE: Bellingham, WA, USA, 2016; Volume 9904, pp. 20–33. [\[CrossRef\]](#)
133. Corbacho, V.V.; Kuiper, H.; Gill, E. Review on thermal and mechanical challenges in the development of deployable space optics. *J. Astron. Telesc. Instruments, Syst.* **2020**, *6*, 1–30. [\[CrossRef\]](#)
134. Barba, M.; Bruce, R.; Bonelli, A.; Baudouy, B. Experimental study of Large-scale cryogenic Pulsating Heat Pipe. *IOP Conf. Ser. Mater. Sci. Eng.* **2017**, *278*, 012156. [\[CrossRef\]](#)
135. Bruce, R.; Barba, M.; Bonelli, A.; Baudouy, B. Thermal performance of a meter-scale horizontal nitrogen Pulsating Heat Pipe. *Cryogenics* **2018**, *93*, 66–74. [\[CrossRef\]](#)
136. Barba, M.; Bruce, R.; Bouchet, F.; Bonelli, A.; Baudouy, B. Effects of filling ratio of a long cryogenic Pulsating Heat Pipe. *Appl. Therm. Eng.* **2021**, *194*, 117072. [\[CrossRef\]](#)
137. Barba, M.; Bruce, R.; Bouchet, F.; Bonelli, A.; Baudouy, B. Effect of the thermo-physical properties of the working fluid on the performance of a 1-m long cryogenic horizontal pulsating heat pipe. *Int. J. Heat Mass Transf.* **2022**, *187*, 122458. [\[CrossRef\]](#)
138. Prest, M.; Barbiellini, G.; Bordignon, G.; Fedel, G.; Liello, F.; Longo, F.; Pontoni, C.; Vallazza, E. The AGILE silicon tracker: An innovative  $\gamma$ -ray instrument for space. *Nucl. Instrum. Methods Phys. Res. Sect. A Accel. Spectrometers Detect. Assoc. Equip.* **2003**, *501*, 280–287. [\[CrossRef\]](#)
139. Atwood, W.; Bagagli, R.; Baldini, L.; Bellazzini, R.; Barbiellini, G.; Belli, F.; Borden, T.; Brez, A.; Brigida, M.; Caliendo, G.; et al. Design and initial tests of the Tracker-converter of the Gamma-ray Large Area Space Telescope. *Astropart. Phys.* **2007**, *28*, 422–434. [\[CrossRef\]](#)
140. Tykhonov, A.; Ambrosi, G.; Asfandiyarov, R.; Azzarello, P.; Bernardini, P.; Bertucci, B.; Bolognini, A.; Cadoux, F.; D'Amone, A.; De Benedittis, A.; et al. In-flight performance of the DAMPE silicon tracker. *Nucl. Instrum. Methods Phys. Res. Sect. A Accel. Spectrometers Detect. Assoc. Equip.* **2019**, *924*, 309–315. [\[CrossRef\]](#)



141. Turchetta, R. Spatial resolution of silicon microstrip detectors. *Nucl. Instrum. Methods Phys. Res. Sect. A Accel. Spectrometers Detect. Assoc. Equip.* **1993**, *335*, 44–58. [[CrossRef](#)]
142. Straulino, S.; Adriani, O.; Bonechi, L.; Bongi, M.; Bottai, S.; Castellini, G.; Fedele, D.; Grandi, M.; Papini, P.; Ricciarini, S.B.; et al. Spatial resolution of double-sided silicon microstrip detectors for the PAMELA apparatus. *Nucl. Instrum. Methods Phys. Res. Sect. A Accel. Spectrometers Detect. Assoc. Equip.* **2006**, *556*, 100–114. [[CrossRef](#)]
143. Ambrosi, G.; Choutko, V.; Delgado, C.; Oliva, A.; Yan, Q.; Li, Y. The spatial resolution of the silicon tracker of the Alpha Magnetic Spectrometer. *Nucl. Instrum. Methods Phys. Res. Sect. A Accel. Spectrometers Detect. Assoc. Equip.* **2017**, *869*, 29–37. [[CrossRef](#)]
144. Ambrosi, G.; Azzrello, P.; Battiston, R.; Bazo, J.; Bertucci, B.; Choumilov, E.; Choutko, V.; Delgado-Mendez, C.; Duranti, M.; D'Urso, D.; et al. Alignment of the AMS-02 silicon Tracker. In Proceedings of the International Cosmic Ray Conference—PoS(ICRC2013), Rio de Janeiro, Brazil, 2–9 July 2013; Volume 33, p. 570.
145. IDE1140. 2021. Available online: <http://ideas.no/products/ide1140/> (accessed on 13 January 2022).
146. Jia, Y.; Yan, Q.; Choutko, V.; Liu, H.; Oliva, A. Nuclei charge measurement by the Alpha Magnetic Spectrometer silicon tracker. *Nucl. Instrum. Methods Phys. Res. Sect. A Accel. Spectrometers Detect. Assoc. Equip.* **2020**, *972*, 164169. [[CrossRef](#)]
147. Cartiglia, N.; Baselga, M.; Dellacasa, G.; Ely, S.; Fadeyev, V.; Galloway, Z.; Garbolino, S.; Marchetto, F.; Martoiu, S.; Mazza, G.; et al. Performance of ultra-fast silicon detectors. *J. Instrum.* **2014**, *9*, C02001. [[CrossRef](#)]
148. Duranti, M.; Vagelli, V.; Ambrosi, G.; Barbanera, M.; Bertucci, B.; Catanzani, E.; Donnini, F.; Faldi, F.; Formato, V.; Graziani, M.; et al. Advantages and Requirements in Time Resolving Tracking for Astroparticle Experiments in Space. *Instruments* **2021**, *5*, 20. [[CrossRef](#)]
149. Weeroc. 2021. Available online: <https://www.weeroc.com/products/sipm-read-out/petiroc-2a>, (accessed on 25 January 2022).
150. Turchetta, R.; Berst, J.; Casadei, B.; Claus, G.; Colledani, C.; Dulinski, W.; Hu, Y.; Husson, D.; Le Normand, J.; Riester, J.; et al. A monolithic active pixel sensor for charged particle tracking and imaging using standard VLSI CMOS technology. *Nucl. Instrum. Methods Phys. Res. Sect. A Accel. Spectrometers Detect. Assoc. Equip.* **2001**, *458*, 677–689. [[CrossRef](#)]
151. Yang, P.; Aglieri, G.; Cavicchioli, C.; Chalmet, P.; Chanlek, N.; Collu, A.; Gao, C.; Hillemanns, H.; Junique, A.; Kofarago, M.; et al. Low-power priority Address-Encoder and Reset-Decoder data-driven readout for Monolithic Active Pixel Sensors for tracker system. *Nucl. Instrum. Methods Phys. Res. Sect. A Accel. Spectrometers Detect. Assoc. Equip.* **2015**, *785*, 61–69. [[CrossRef](#)]
152. Mager, M. ALPIDE, the Monolithic Active Pixel Sensor for the ALICE ITS upgrade. *Nucl. Instrum. Methods Phys. Res. Sect. A Accel. Spectrometers Detect. Assoc. Equip.* **2016**, *824*, 434–438. [[CrossRef](#)]
153. Aglieri, G.; Cavicchioli, C.; Chalmet, P.L.; Chanlek, N.; Collu, A.; Giubilato, P.; Hillemanns, H.; Junique, A.; Keil, M.; Kim, D.; et al. Monolithic active pixel sensor development for the upgrade of the ALICE inner tracking system. *J. Instrum.* **2013**, *8*, C12041. [[CrossRef](#)]
154. Mager, M. Upgrade of the ALICE ITS in LS3. In Proceedings of the 28th International Workshop on Vertex Detectors—PoS(Vertex2019), Lopud, Croatia, 13–18 October 2019; Volume 373, p. 40. [[CrossRef](#)]
155. Neubüser, C.; Corradino, T.; Dalla Betta, G.F.; De Cilladi, L.; Pancheri, L. Sensor Design Optimization of Innovative Low-Power, Large Area FD-MAPS for HEP and Applied Science. *Front. Phys.* **2021**, *9*, 639. [[CrossRef](#)]
156. De Santis, C.; Ricciarini, S. The High Energy Particle Detector (HEPD-02) for the second China Seismo-Electromagnetic Satellite (CSES-02). In Proceedings of the 37th International Cosmic Ray Conference—PoS(ICRC2021), Berlin, Germany, 12–23 July 2021; Volume 395, p. 58. [[CrossRef](#)]
157. Ricciarini, S.B.; Beolé, S.; de Cilladi, L.; Gebbia, G.; Iuppa, R.; Ricci, E.; Zuccon, P. Enabling low-power MAPS-based space trackers: A sparsified readout based on smart clock gating for the High Energy Particle Detector HEPD-02. In Proceedings of the 37th International Cosmic Ray Conference—PoS(ICRC2021), Berlin, Germany, 12–23 July 2021; Volume 395, p. 071. [[CrossRef](#)]
158. Turecek, D.; Pinsky, L.; Jakubek, J.; Vykydal, Z.; Stoffle, N.; Pospisil, S. Small Dosimeter based on Timepix device for International Space Station. *J. Instrum.* **2011**, *6*, C12037–C12037. [[CrossRef](#)]
159. Adriani, O.; Albergo, S.; Auditore, L.; Basti, A.; Berti, E.; Bigongiari, G.; Bonechi, L.; Bonechi, S.; Bongi, M.; Bonvicini, V.; et al. CaloCube: An isotropic spaceborne calorimeter for high-energy cosmic rays. Optimization of the detector performance for protons and nuclei. *Astropart. Phys.* **2017**, *96*, 11–17. [[CrossRef](#)]
160. Adriani, O.; Albergo, S.; Auditore, L.; Basti, A.; Berti, E.; Bigongiari, G.; Bonechi, L.; Bongi, M.; Bonvicini, V.; Bottai, S.; et al. The CALOCUBE project for a space based cosmic ray experiment: Design, construction, and first performance of a high granularity calorimeter prototype. *J. Instrum.* **2019**, *14*, P11004. [[CrossRef](#)]
161. Adriani, O.; Agnesi, A.; Albergo, S.; Antonelli, M.; Auditore, L.; Basti, A.; Berti, E.; Bigongiari, G.; Bonechi, L.; Bongi, M.; et al. The CaloCube calorimeter for high-energy cosmic-ray measurements in space: Performance of a large-scale prototype. *J. Instrum.* **2021**, *16*, P10024. [[CrossRef](#)]
162. Pacini, L.; Adriani, O.; Bai, Y.L.; Bao, T.W.; Berti, E.; Bottai, S.; Cao, W.W.; Casaus, J.; Cui, X.Z.; D'Alessandro, R.; et al. Design and expected performances of the large acceptance calorimeter for the HERD space mission. In Proceedings of the 37th International Cosmic Ray Conference—PoS(ICRC2021), Berlin, Germany, 12–23 July 2021; Volume 395, p. 66. [[CrossRef](#)]
163. Zhang, L.; Mao, R.; Yang, F.; Zhu, R.Y. LSO/LYSO Crystals for Calorimeters in Future HEP Experiments. *IEEE Trans. Nucl. Sci.* **2014**, *61*, 483–488. [[CrossRef](#)]
164. Vitale, V. The Limadou-HEPD Segmented Calorimeter. *EPJ Web Conf.* **2019**, *209*, 1034. [[CrossRef](#)]



165. Barbato, F.; Abba, A.; Anastasio, A.; Barbarino, G.; Boiano, A.; de Asmundis, R.; De Mitri, I.; Ferrentino, L.; Garufi, F.; Guarino, F.; et al. The Crystal Eye X and gamma ray detector for space missions. In Proceedings of the 37th International Cosmic Ray Conference—PoS(ICRC2021), Berlin, Germany, 12–23 July 2021; Volume 395, p. 581. [\[CrossRef\]](#)
166. Bonvicini, V.; Orzan, G.; Zampa, G.; Zampa, N. A Double-Gain, Large Dynamic Range Front-end ASIC With A/D Conversion for Silicon Detectors Read-Out. *IEEE Trans. Nucl. Sci.* **2010**, *57*, 2963–2970. [\[CrossRef\]](#)
167. Böhlen, T.; Cerutti, F.; Chin, M.; Fassò, A.; Ferrari, A.; Ortega, P.; Mairani, A.; Sala, P.; Smirnov, G.; Vlachoudis, V. The FLUKA Code: Developments and Challenges for High Energy and Medical Applications. *Nucl. Data Sheets* **2014**, *120*, 211–214. [\[CrossRef\]](#)
168. Bigongiari, G.; Adriani, O.; Albergo, S.; Ambrosi, G.; Auditore, L.; Basti, A.; Berti, E.; Bonechi, L.; Bonechi, S.; Bonghi, M.; et al. A New Approach to Calorimetry in Space-Based Experiments for High-Energy Cosmic Rays. *Universe* **2019**, *5*, 72. [\[CrossRef\]](#)
169. Osteria, G.; Campana, D.; Barbarino, G.; Boscherini, M.; Menn, W.; Mitchell, J.; Rossi, G.; Russo, S.; Simon, M.; Streitmatter, R. The time-of-flight system of the PAMELA experiment on satellite. *Nucl. Instrum. Methods Phys. Res. Sect. A Accel. Spectrometers Detect. Assoc. Equip.* **2004**, *535*, 152–157. [\[CrossRef\]](#)
170. Bindi, V.; Chen, G.; Chen, H.; Choumilov, E.; Choutko, V.; Contin, A.; Lebedev, A.; Lu, Y.; Masi, N.; Oliva, A.; et al. Calibration and performance of the AMS-02 time of flight detector in space. *Nucl. Instrum. Methods Phys. Res. Sect. A Accel. Spectrometers Detect. Assoc. Equip.* **2014**, *743*, 22–29. [\[CrossRef\]](#)
171. Renker, D.; Lorenz, E. Advances in solid state photon detectors. *J. Instrum.* **2009**, *4*, P04004. [\[CrossRef\]](#)
172. Piemonte, C.; Gola, A. Overview on the main parameters and technology of modern Silicon Photomultipliers. *Nucl. Instrum. Methods Phys. Res. Sect. A Accel. Spectrometers Detect. Assoc. Equip.* **2019**, *926*, 2–15. [\[CrossRef\]](#)
173. Ambrosi, G.; Vagelli, V. Applications of silicon photomultipliers in ground-based and spaceborne high-energy astrophysics. *Eur. Phys. J. Plus* **2022**, *137*, 170. [\[CrossRef\]](#)
174. Link, J.; Brandt, T.; De Nolfo, G.A.; Du Monthier, J.; Krizmanic, J.; Mitchell, J.; Mitchell, S.; Sakai, K.; Sasaki, M.; Suarez, G.; et al. SiPM use in Future Space Instruments. In Proceedings of the 35th International Cosmic Ray Conference—PoS(ICRC2017), Bexco, Korea, 12–20 July 2017; Volume 301, p. 235. [\[CrossRef\]](#)
175. Quinn, S. The GAPS Instrument: A Large Area Time of Flight and High Resolution Exotic Atom Spectrometer for Cosmic Antinuclei. In Proceedings of the 37th International Cosmic Ray Conference—PoS(ICRC2021), Berlin, Germany, 12–23 July 2021; Volume 395, p. 79. [\[CrossRef\]](#)
176. Wang, J.j.; Wu, X.; Xu, M.; Perrina, C.; Azzarello, P.; Cadoux, F.; Favre, Y.; Marra, D.L.; Wu, B.b. Feasibility study of cosmic-ray components measurement by using a scintillating fiber tracker in space. *Radiat. Detect. Technol. Methods* **2021**, *5*, 389–403. [\[CrossRef\]](#)
177. Altomare, C.; De La Torre Luque, P.; Di Venere, L.; Fusco, P.; Gargano, F.; Giordano, F.; Hu, P.; Loparco, F.; Loporchio, S.; Mazziotto, M.; et al. Particle identification capability of Plastic scintillator tiles equipped with SiPMs for the High Energy cosmic-Radiation Detection (HERD) facility. *Nucl. Instrum. Methods Phys. Res. Sect. A Accel. Spectrometers Detect. Assoc. Equip.* **2020**, *983*, 164476. [\[CrossRef\]](#)
178. Betancourt, C.; Blondel, A.; Brundler, R.; Dätwyler, A.; Favre, Y.; Gascon, D.; Gomez, S.; Korzenev, A.; Mermoud, P.; Noah, E.; et al. Application of large area SiPMs for the readout of a plastic scintillator based timing detector. *J. Instrum.* **2017**, *12*, P11023. [\[CrossRef\]](#)
179. Betancourt, C.; Dätwyler, A.; Serra, N.; Storaci, B.; Blondel, A.; Korzenev, A.; Mermoud, P.; Noah, E.; Gascon, D.; Gomez, S. A timing detector for the SHiP experiment. *Nucl. Instrum. Methods Phys. Res. Sect. A Accel. Spectrometers Detect. Assoc. Equip.* **2019**, *924*, 369–372. [\[CrossRef\]](#)
180. Cattaneo, P.W.; De Gerone, M.; Gatti, F.; Nishimura, M.; Ootani, W.; Rossella, M.; Uchiyama, Y. Development of High Precision Timing Counter Based on Plastic Scintillator with SiPM Readout. *IEEE Trans. Nucl. Sci.* **2014**, *61*, 2657–2666. [\[CrossRef\]](#)
181. Böhm, M.; Götzen, K.; Gruber, L.; Kratochwil, N.; Lehmann, A.; Orth, H.; Steinschaden, D.; Suzuki, K.; Zimmermann, S. The PANDA Barrel-TOF Detector. *Nucl. Instrum. Methods Phys. Res. Sect. A Accel. Spectrometers Detect. Assoc. Equip.* **2018**, *912*, 323–325. [\[CrossRef\]](#)
182. Chung, C.; Backes, T.; Dittmar, C.; Karpinski, W.; Kirn, T.; Louis, D.; Schwering, G.; Wlochal, M.; Schael, S. The Development of SiPM-Based Fast Time-of-Flight Detector for the AMS-100 Experiment in Space. *Instruments* **2022**, *6*, 14. [\[CrossRef\]](#)
183. Paternoster, G. Silicon Photomultipliers developed at FBK for Physics Applications. In Proceedings of the Contribution to 13th Trento Workshop on Advanced Silicon Radiation Detectors, Munich, Germany, 19–21 February 2018.
184. Garutti, E.; Musienko, Y. Radiation damage of SiPMs. *Nucl. Instrum. Methods Phys. Res. A* **2019**, *926*, 69–84.
185. Durante, M.; Cucinotta, F.A. Physical basis of radiation protection in space travel. *Rev. Mod. Phys.* **2011**, *83*, 1245–1281. [\[CrossRef\]](#)
186. Link, J.; Akaike, Y.R.; Binns, W.G.; Bose, R.J.; Brandt, T.H.; Buckley, J. O.; Cannady, S.A.; De Nolfo, G F.; Dowkontt, P.J.; Du Monthier, J.; et al. Silicon Photomultiplier use in Particle Astrophysics and Heliophysics Missions. In Proceedings of the 36th International Cosmic Ray Conference —PoS(ICRC2019), Madison, WI, USA, 24 July–1 August 2019; Volume 358, p. 096. [\[CrossRef\]](#)
187. Altamura, A.R.; Acerbi, F.; Ruzza, B.D.; Verroi, E.; Merzi, S.; Gola, A. Radiation damage on SiPMs for Space Applications. *arXiv* **2021**, arXiv:physics.ins-det/2112.08089.
188. Kim, M.; Bagliesi, M.; Bigongiari, G.; Bonechi, S.; Marrocchesi, P.; Maestro, P. Beam test performance of SiPM-based detectors for cosmic-ray experiments. *Nucl. Instrum. Methods Phys. Res. Sect. A Accel. Spectrometers Detect. Assoc. Equip.* **2013**, *703*, 177–182. [\[CrossRef\]](#)

189. Marrocchesi, P.S.; Bagliesi, M.G.; Bonechi, S.; Bigongiari, G.; Brogi, P.; Collazuol, G.; Ferri, A.; Maestro, P.; Piemonte, C.; Sulaj, A.; et al. Charged Particle Detection with NUV-Sensitive SiPM in a Beam of Relativistic Ions. *IEEE Trans. Nucl. Sci.* **2014**, *61*, 2786–2793. [CrossRef]
190. Otte, A.N.; Garcia, D.; Nguyen, T.; Purushotham, D. Characterization of three high efficiency and blue sensitive silicon photomultipliers. *Nucl. Instrum. Methods Phys. Res. Sect. A Accel. Spectrometers Detect. Assoc. Equip.* **2017**, *846*, 106–125. [CrossRef]
191. Licciulli, F.; Marzocca, C. An Active Compensation System for the Temperature Dependence of SiPM Gain. *IEEE Trans. Nucl. Sci.* **2015**, *62*, 228–235. [CrossRef]
192. Kuznetsov, E. Temperature-compensated silicon photomultiplier. *Nucl. Instrum. Methods Phys. Res. Sect. A Accel. Spectrometers Detect. Assoc. Equip.* **2018**, *912*, 226–230. [CrossRef]
193. Ahmad, S.; Fleury, J.; de la Taille, C.; Seguin-Moreau, N.; Dulucq, F.; Martin-Chassard, G.; Callier, S.; Thienpont, D.; Raux, L. Triroc: A Multi-Channel SiPM Read-Out ASIC for PET/PET-ToF Application. *IEEE Trans. Nucl. Sci.* **2015**, *62*, 664–668. [CrossRef]
194. Weeroc. 2021. Available online: <https://www.weeroc.com/products/sipm-read-out/petiroc-2ax> (accessed on 1 April 2022).
195. Ahmad, S.; Blin, S.; Callier, S.; Cizel, J.B.; Conforti, S.; de La Taille, C.; Dulucq, F.; Fleury, J.; Martin-Chassard, G.; Raux, L.; et al. OMEGA SiPM readout ASICs. *Nucl. Instrum. Methods Phys. Res. Sect. A Accel. Spectrometers Detect. Assoc. Equip.* **2021**, *986*, 164628. [CrossRef]
196. Fleury, J.; Ahmad, S.; de La Taille, C.; Callier, S.; Raux, L. LIROC : Novative RadHard Front-End ASIC for Lidar, 2020. In Proceedings of the Public Deliverable for the ATTRACT Final Conference, Online, 22–23 September 2020.
197. Perez, K.; von Doetinchem, P.; Aramaki, T.; Boezio, M.; Boggs, S.E.; Craig, W.W.; Fabris, L.; Fuke, H.; Gahbauer, F.; Hailey, C.J.; et al. Astro 2020 Science White Paper: Cosmic-ray Antinuclei as Messengers for Dark Matter. *arXiv* **2021**, arXiv:astro-ph.HE/1904.05938.
198. Andronic, A.; Wessels, J. Transition radiation detectors. *Nucl. Instrum. Methods Phys. Res. Sect. A Accel. Spectrometers Detect. Assoc. Equip.* **2012**, *666*, 130–147. [CrossRef]
199. Artru, X.; Yodh, G.B.; Mennessier, G. Practical theory of the multilayered transition radiation detector. *Phys. Rev. D* **1975**, *12*, 1289–1306. [CrossRef]
200. Brigida, M.; Favuzzi, C.; Fusco, P.; Gargano, F.; Giglietto, N.; Giordano, F.; Loparco, F.; Marangelli, B.; Mazziotta, M.; Mirizzi, N.; et al. Investigation of the transition radiation produced by fast electrons crossing multifoil and fiber radiators. *Nucl. Instrum. Methods Phys. Res. Sect. A Accel. Spectrometers Detect. Assoc. Equip.* **2005**, *550*, 157–168. [CrossRef]
201. Brigida, M.; Favuzzi, C.; Fusco, P.; Gargano, F.; Giglietto, N.; Giordano, F.; Loparco, F.; Marangelli, B.; Mazziotta, M.; Mirizzi, N.; et al. A Silicon Transition Radiation Detector for space and accelerator applications. *Nucl. Instrum. Methods Phys. Res. Sect. A Accel. Spectrometers Detect. Assoc. Equip.* **2006**, *564*, 115–125. [CrossRef]
202. Brigida, M.; Caliendo, G.; Favuzzi, C.; Fusco, P.; Gargano, F.; Giglietto, N.; Giordano, F.; Loparco, F.; Marangelli, B.; Mazziotta, M.; et al. Beam test results with a reduced scale Silicon Transition Radiation Detector prototype. *Nucl. Instrum. Methods Phys. Res. Sect. A Accel. Spectrometers Detect. Assoc. Equip.* **2007**, *577*, 519–522. [CrossRef]
203. Golden, R.L.; Stochaj, S.J.; Stephens, S.A.; Aversa, F.; Barbiellini, G.; Boezio, M.; Bravar, U.; Colavita, A.; Fratnik, F.; Schiavon, P.; et al. Measurement of the Positron to Electron Ratio in the Cosmic Rays above 5 GeV. *Astrophys. J.* **1996**, *457*. [CrossRef]